

# The Role of the Guide Field in Relativistic Pair Plasma Reconnection

S. Zenitani

*NASA Goddard Space Flight Center, Greenbelt, MD 20771;  
zenitani@lssp-mail.gsfc.nasa.gov*

M. Hoshino

*Department of Earth and Planetary Science, University of Tokyo, 7-3-1, Hongo, Bunkyo,  
Tokyo, 113-0033 Japan*

## ABSTRACT

We study the role of the guide field in relativistic magnetic reconnection in a Harris current sheet of pair ( $e^\pm$ ) plasmas, using linear theories and particle-in-cell (PIC) simulations. Two-dimensional PIC simulations exhibit the guide field dependence to the linear instabilities; the tearing or reconnection modes are relatively insensitive, while the relativistic drift-kink instability (RDKI), the fastest mode in a relativistic current sheet, is stabilized by the guide field. Particle acceleration in the nonlinear stage is also investigated. A three-dimensional PIC simulation demonstrates that the current sheet is unstable to the RDKI, although a small reconnection occurs in the deformed current sheet. Another three-dimensional PIC simulation with a guide field demonstrates a completely different scenario. Secondary magnetic reconnection is triggered by nonlinear coupling of oblique instabilities, which we call the relativistic drift-sausage tearing instability. Therefore, particle acceleration by relativistic guide field reconnection occurs in three-dimensional configuration. Based on the plasma theories, we discuss an important role of the guide field: to enable non-thermal particle acceleration by magnetic reconnection.

*Subject headings:* acceleration of particles — magnetic fields — plasmas — instabilities — relativity

## 1. INTRODUCTION

Magnetic reconnection in collisionless plasmas is of strong interest in high-energy astrophysical places such as active galactic nuclei (AGNs; di Matteo (1998); Birk et al. (2001)),

extragalactic jets (Romanova & Lovelace 1992; Lesch & Birk 1998; Larrabee et al. 2003), pulsar winds (Michel 1982, 1994; Coroniti 1990; Lyubarsky & Kirk 2001; Kirk & Skjæraasen 2003), gamma-ray bursts (Drenkhahn 2002; Drenkhahn & Spruit 2002; Uzdensky & MacFadyen 2006) and, soft gamma repeaters (Thompson & Duncan 1995, 2001; Lyutikov 2003, 2006). Since it rapidly releases stored magnetic energy into plasma kinetic energy, reconnection is considered as a possible underlying mechanism, to explain particle acceleration or bursty emission signatures in these sites, regardless of plasma composition (pair plasmas or ion-electron plasmas).

For instance, in the case of the Crab pulsar, magnetic reconnection is considered in the relativistic radial outflow of pair plasmas. Since the central neutron star is a fast oblique rotator, its strong magnetic fields ( $\sim 10^{12}$  G) are highly striped so that field lines are almost toroidal inside the flow. Magnetic reconnection is expected to occur in field reversal configuration of toroidal fields, in order to dissipate the magnetic energy (Coroniti 1990). In the AGN context, magnetic reconnection is expected in association with magnetic loops from a differentially rotating acceleration disk. In this situation, the field configuration involves magnetic fields perpendicular to the antiparallel component. Indeed, reconnection in sheared configuration is proposed as an acceleration site of MeV/GeV electrons (Lesch & Birk 1997; Schopper et al. 1998; Nodes et al. 2003), due to the field-aligned electric field  $E_{\parallel}$ . In the case of soft gamma repeaters, a giant flare is expected in ultrastrong magnetic environment ( $\sim 10^{15}$  G) around central neutron stars (magnetars). Although there are various theoretical models, it is expected that giant flares involve magnetic reconnection in the relativistic pair plasma environment.

However, the fundamental mechanism of relativistic magnetic reconnection, as well as the conventional non-relativistic counterpart, is far from being understood. From the magnetohydrodynamics (MHD) viewpoint, steady state reconnection models have been extended to the relativistic regime (Blackman & Field 1994; Lyutikov & Uzdensky 2003; Lyubarsky 2005), although they do not fully agree. The relativistic resistive MHD simulation demonstrated mildly-relativistic Petschek reconnection (Watanabe & Yokoyama 2006). From the kinetic viewpoint, series of particle-in-cell (PIC) simulations demonstrated that relativistic magnetic reconnection is a powerful acceleration engine (Zenitani & Hoshino 2001, 2005b, 2007; Jaroschek et al. 2004b), primarily due to the direct particle acceleration by the reconnection electric field, which is perpendicular to the reconnecting magnetic field lines. In fact, obtained plasma energy distribution is highly non-thermal, approximated by the power-law distribution with an index of  $-1 \sim -3$  (Romanova & Lovelace 1992; Zenitani & Hoshino 2001; Larrabee et al. 2003; Jaroschek et al. 2004b). Thus, magnetic reconnection seems to be a favorable source of non-thermal particles at the sites of synchrotron radiation (Jaroschek et al. 2004a). However, it was reported that the current sheet configuration is unstable to

the relativistic drift kink instability (hereafter the RDKI), which occurs in the plane perpendicular to the reconnection plane (Zenitani & Hoshino 2005a). The RDKI grows more rapidly than reconnection, and it mainly contributes to plasma heating (Zenitani & Hoshino 2007). Thus, plasma heating by the RDKI overwrites the reconnection scenario; nonthermal particle acceleration is unlikely to occur in antiparallel field configuration in relativistically hot pair plasmas.

Pair plasma reconnection has also attracted recent attention as an equal-mass-limit example of ion-electron reconnection. For example, there is a long-standing problem regarding the reason collisionless reconnection occurs “faster” than predicted by the MHD theories. It has been widely argued that Hall physics plays an essential role in maintaining fast reconnection (the GEM reconnection challenge; Birn et al. (2001); Shay et al. (2001)), but fast reconnection in non-relativistic pair plasma shows a counter-evidence because it does not involve Hall effects (Bessho & Bhattacharjee 2005). Instead, although its physical interpretation needs refinement, it seems that the off-diagonal part of the pressure tensor (Hesse et al. 1999) accounts for the electric field for fast reconnection (Bessho & Bhattacharjee 2007; Hesse & Zenitani 2007). Furthermore, it has recently been argued that late-time dynamical structure may regulate fast reconnection (Daughton & Karimabadi 2007).

Guide field configuration, which contains a perpendicular magnetic field to the antiparallel components, is an important generalization for studying the reconnection problem in a shear or twisted configuration. Reconnection with the uniform guide field has long been studied for better understanding of the reconnection structure (Drake & Lee 1977; Katanuma & Kamimura 1980; Hoshino 1987; Horiuchi & Sato 1997; Hesse et al. 1999, 2004) and for applications to solar flares and to the Earth’s magnetopause (Shibata et al. 1995; Quest & Coroniti 1981; Sonnerup et al. 1981). Recent three-dimensional (3D) PIC simulations (Scholer et al. 2003; Drake et al. 2003; Ricci et al. 2003; Silin & Büchner 2003; Pritchett & Coroniti 2004) discussed reduction of the cross-field activities (Scholer et al. 2003; Silin & Büchner 2003), detailed reconnection region structure (Pritchett & Coroniti 2004), and enhanced electron acceleration (Drake et al. 2003; Ricci et al. 2003). We note that the acceleration mechanism differs from the one in the antiparallel counterpart because the reconnection electric field is no longer perpendicular to magnetic lines; guide field reconnection involves a parallel electric field  $E_{\parallel}$  to accelerate electrons (Ricci et al. 2003). In relativistic pair plasmas, Zenitani & Hoshino (2005b) presented the idea that the guide field stabilizes the RDKI and that the new oblique instability triggers secondary magnetic reconnection. Nonthermal particle acceleration by magnetic reconnection seems to be a likely process in a relativistic current sheet once again, under the guide field condition.

The purpose of this paper is to comprehensively discuss the role of the guide field

in relativistic pair plasma reconnection. Extending our recent papers (Zenitani & Hoshino (2005b) and Zenitani & Hoshino (2007), hereafter referred as ZH05b and ZH07, respectively), we investigate the linear and non-linear development of a relativistic current sheet in pair plasmas, by using fully self-consistent kinetic PIC simulations. The conclusion of this paper is that relativistic guide field reconnection is a favorable process for nonthermal particle acceleration, from the viewpoint of detailed plasma theory.

This paper consists of the following sections. In §2 we describe the simulation setup. In §3 we study the two-dimensional evolution of the current sheet with the guide field. We investigate how the guide field affects the linear instabilities in §3.1, and then we study how particles are accelerated in nonlinear guide field reconnection in §3.2. In §4, we study the 3D evolution of an anti-parallel current sheet. In §5, we study the 3D evolution of a current sheet with a guide field. We introduce new linear instabilities in the oblique directions in §5.1, and then we discuss the nonlinear development of the current sheet in §5.2, in relevance to the two-dimensional counterparts. Section 6 contains discussion and the summary.

## 2. SIMULATION MODEL

Throughout this study, we employ a relativistic Harris model as an initial configuration. Magnetic field and plasma distribution functions are set in the following way:

$$\mathbf{B} = B_0 \tanh(z/\lambda) \hat{\mathbf{x}} + \alpha B_0 \hat{\mathbf{y}}, \quad (1)$$

$$f_s = \frac{n_0 \cosh^{-2}(z/\lambda)}{4\pi m^2 c T K_2(mc^2/T)} \exp\left[\frac{-\gamma_s(\varepsilon - \beta_s m c u_y)}{T}\right] + \frac{n_{bg}}{4\pi m^2 c T_{bg} K_2(mc^2/T_{bg})} \exp\left[-\frac{\varepsilon}{T_{bg}}\right], \quad (2)$$

where  $B_0$  is the antiparallel magnetic fields,  $\alpha$  is the relative amplitude of the guide field,  $n_0$  is the plasma number density of the current sheet in the proper frame,  $T$  is the plasma temperature including the Boltzmann constant in the proper frame,  $m$  is the positron/electron mass,  $c$  is the light speed,  $K_2(x)$  is the modified Bessel function of the second kind, the subscript  $s$  denotes the species ( $p$  for positrons and  $e$  for electrons),  $c\beta_s$  is the drift speed of the species, and  $u$  is the four velocity. The parameters  $T$  and  $n_0$  are defined in the proper frame.  $T_{bg}$  and  $n_{bg}$  are the temperature and the number density of background plasmas. In this paper, we choose  $\beta_p = 0.3$ ,  $\beta_e = -0.3$  (relevant Lorentz factor is  $\gamma_\beta = 1.048$ ),  $T/mc^2 = 1$ ,  $T_{bg}/T = 0.1$  and  $n_{bg}/(\gamma_\beta n_0) = 0.05$ . Notice that the Harris model with the uniform guide field exactly satisfies an equilibrium. We assume that  $B_y$  is negative, but we will observe the same (mirror) results in the positive cases, because of the mathematical symmetry in pair plasmas. We use 3D particle-in-cell (PIC) code with periodic boundaries in all three directions. Because of the field reversal, we set double current sheets in the  $z$  direction. The

typical scale of the current sheet  $\lambda$  is set to 10 grids. The size of the simulation box depends on the problem. Their sizes are presented in Table 1. These conditions are same as our recent studies; runs R3 and D3 are identical to ones in ZH07 and runs 3D-A and 3D-B are identical to run A and run B in ZH05b.

In many cases, we impose small artificial electric fields around  $(x, y, z) = (0, 0, \pm 3\lambda)$  in the very early stage of simulation runs, in order to “force” reconnection around the center of the main simulation domain. Typical spatial ranges for the artificial fields are set to  $(\Delta x, \Delta z) \sim (\pm 2\lambda, \pm \lambda)$  in two-dimensional cases and  $(\Delta x, \Delta y, \Delta z) \sim (\pm 2\lambda, \pm 2\lambda, \pm \lambda)$  in 3D cases. This force is often strong enough and then reconnection process immediately breaks up soon after short linear growth stage. In Table 1, the letter F means that we observe such sudden breakup of forced reconnection. S\* means that we observe quasi-spontaneous evolution, because the trigger force is not strong enough. In these cases, it takes some time until nonlinear reconnection breaks up, and we observe the linear growth of the instabilities for a while. In S cases, we set no trigger force. In two-dimensional runs for the RDKI, we do not need the trigger force because the instability quickly grows from thermal noise.

### 3. GUIDE FIELD EFFECT TO THE TWO-DIMENSIONAL PROCESSES

#### 3.1. Linear Growth Rates

First, we investigate the guide field effect on the two-dimensional reconnection instabilities: relativistic reconnection in the  $x$ - $z$  plane and the RDKI in the  $y$ - $z$  plane. We carry out a series of two-dimensional simulations: five cases of reconnection ( $\alpha = B_y/B_0 = 0, -0.5, -1, -1.5, -5$ ) and four cases of the RDKI ( $B_y/B_0 = 0, -0.25, -0.5, -1$ ). Then, we calculate the linear growth rates of the fastest growing modes from the perturbed magnetic fields  $\delta \mathbf{B}$  in the neutral plane. In reconnection cases, it is sometimes difficult to pick up the “linear” mode, because the linear stage is rather short. It seems that the linear stage takes longer time, when the initial artificial impact is zero or weak. Therefore, for the most difficult case of  $B_y/B_0 = -1.5$  (run R3-C), we also carry out the relevant spontaneous run (run R3-D) to confirm the linear growth rate. We notice that the linear growth rate is not identical to the energy release rates in the nonlinear stage. Once the nonlinear reconnection breaks up, the linear perturbations quickly cascade into the longer-wavelength perturbations, which grows more explosively, 2-3 times faster than the linear or quasi-linear modes.

Along with the PIC simulations, we evaluate the linear growth rates of the two-dimensional instabilities by using eigenvalue analysis, in the same way as our previous work (Appendix

B in ZH07). In this analysis, we use the relativistic fluid equations

$$\frac{\gamma_s^2}{c^2}(p_s + e_s)\left(\frac{\partial}{\partial t} + \mathbf{v}_s \cdot \nabla\right)\mathbf{v}_s = -\nabla p_s + \gamma_s q_s n_s \left(\mathbf{E} + \frac{\mathbf{v}_s}{c} \times \mathbf{B}\right) - \frac{\mathbf{v}_s}{c^2}(\gamma_s q_s n_s \mathbf{E} \cdot \mathbf{v}_s + \frac{\partial p_s}{\partial t}), \quad (3)$$

where  $p$  is the isotropic plasma pressure and  $e$  is the internal energy that contains the rest mass energy. In addition, we use the continuity, Maxwell equations, and adiabatic gas condition to close equations. We assume the perturbation for arbitrary wavevector  $\mathbf{k} = (k_x, k_y)$ ;  $\delta f \propto \delta f(z) \exp(ik_x x + ik_y y + \omega_i t)$ , where  $\omega_i$  is the linear growth rate (the imaginary part of the wave frequency), and then we solve the linearized equations as an eigenvalue problem.

Let us discuss two-fluid theory in the  $x$ - $z$  plane ( $k_y = 0$  or  $\partial/\partial y = 0$ ). By ignoring the relativistic drift speed effect (third term of the right-hand side of eq. [3]), simple assumptions ( $q_p = -q_e = q$ ,  $\gamma_p = \gamma_e = \gamma$ ,  $p_p = p_e = p$ ,  $e_p = e_e = e$ , and  $n_p = n_e = n$ ) yield the  $y$  component of the generalized Ohm's law

$$\left(\mathbf{E} + \frac{\mathbf{V}}{c} \times \mathbf{B}\right)_y = \frac{\gamma(p + e)}{2c^2 q n} \left(\frac{\partial}{\partial t} v_{py} - \frac{\partial}{\partial t} v_{ey}\right), \quad (4)$$

where  $\mathbf{V} = (1/2)(\mathbf{v}_p + \mathbf{v}_e)$  is the bulk velocity of pair-plasma fluids. This indicates that the fluid inertia of electrons and positrons account for the effective resistivity to break down the frozen-in condition and to drive the tearing instability. The Hall terms are not included, because they vanish in electron-positron plasmas. As discussed in the previous works on the relativistic tearing instability (Zelenyi & Krasnoselskikh 1979) and the conventional tearing instability, we obtain purely-growing modes in the wavevector range of  $0 < k_x \lambda < 1$ . We employ the maximum growth rates in the above parameter range as theoretical eigen growth rates of the reconnection mode. In the  $y$ - $z$  plane ( $k_x = 0$  or  $\partial/\partial x = 0$ ), Daughton (1999) demonstrated that two-fluid theory and Vlasov theory are in good agreement to explain the drift kink instability in ion-electron plasmas, in long-wavelength range of  $k_y \lambda \lesssim 0.7$ . Similarly, we know that our two-fluid theory is in agreement with PIC simulations in long-wavelength range of the RDKI;  $k_y \lambda \lesssim 0.7$  (Zenitani & Hoshino 2005a, 2007). Therefore, we employ  $k_y \lambda = 0.7$  to estimate the typical eigen growth rates of the RDKI. We keep in mind that our theory assumes isotropic fluids and that it does not contain any kinetic effects nor wave-particle interactions. These approximations will break down in a thin current sheet, in which gyro radii is much larger, and so kinetic-based theories are more favorable for describing instabilities (e.g. Vlasov analysis by Brittnacher et al. (1995)). However, in the scope of the present paper, two-fluid theory gives us a plausible estimate of the growth rates.

The obtained growth rates of the reconnection mode are presented in black lines in Figure 1 as a function of  $|B_y/B_0|$ . In PIC simulations, the fastest reconnection mode (Fig. 1, *black line*) has wavenumbers of  $k_x \lambda \sim 0.4$ – $0.7$ , which correspond to those of the relativistic

tearing instability. The maximum eigen growth rates of the relativistic tearing instability are presented with the dashed line in Figure 1. Both growth rates are in agreement. It seems that the growth rates are relatively insensitive to the guide field. In the extreme guide field case ( $|B_y/B_0| = 5.0$ ), the growth rate is still the half of that of the antiparallel case. This tendency is consistent with reconnection studies in ion-electron plasmas; an analysis (Brittnacher et al. 1995) and PIC simulations (Horiuchi & Sato 1997) reported that the linear growth rate decreases by a factor of 2 or 3 under strong guide field conditions (up to  $|B_y/B_0| = 4$ ). It was also reported that the guide field reduces the quasi-steady reconnection rate by a factor of  $\sim 2$  in PIC simulations and Hall MHD simulations (Pritchett & Coroniti 2004; Huba 2005).

The gray lines in Figure 1 show the growth rates of the RDKI (gray line by PIC simulation; gray dashed line by the theory). The RDKI is rather sensitive to the guide field. In PIC simulations, the RDKI spontaneously arises from the thermal noise before  $t/\tau_c = 100$  under no/weak guide field conditions (Runs D3 and D3-A;  $|B_y/B_0| = 0, 0.25$ ). However, we could not observe any sign of the RDKI before  $t/\tau_c = 200$ , when the guide field is strong enough,  $|B_y/B_0| \geq 0.5$ . We also failed to obtain the unstable eigen solutions when guide field amplitude exceeds a threshold;  $|B_y/B_0| \gtrsim (0.45 - 0.5)$ . In the physical sense, since the wavevector is parallel to the guide field lines, the magnetic tension of the guide field prevents the RDKI from growing. Previous ion-electron work (Pritchett & Coroniti 2004) reported that the guide field  $B_y/B_0 = 0.5$  is sufficient to stabilize the kink modes.

In summary, in two-dimensional linear regime, the RDKI grows faster than the reconnection or the relativistic tearing instability under no/weak guide field conditions. However, the situation changes when we introduce a finite amount of the guide field. The reconnection is rather insensitive to the guide field, but the RDKI is suddenly stabilized by the guide field. Therefore, reconnection will dominate in the guide field conditions of  $|B_y/B_0| \gtrsim 0.5$ .

### 3.2. 2D Guide Field Reconnection

Next, we study the nonlinear development of the relativistic guide field reconnection. Among several simulation runs, we present the results of run R3-C ( $|B_y/B_0| = 1.5$ ), in which the guide field features are well developed.

We force magnetic reconnection around the center and then reconnection quickly breaks up. Figure 2 shows snapshots at  $t/\tau_c = 100$ , where  $\tau_c = \lambda/c$  is the light transit time. Figure 2a shows plasma density, average flow and magnetic field lines. The maximum outflow speed is  $\sim 0.37c$  along the  $x$ -axis and it is substantially slower than the antiparallel case of  $\sim (0.7-$

0.8)*c*. The composition of plasma flow depends on the quadrants in the reconnection region; electron flow into the  $(+x, -y)$  direction in the  $(+x, +z)$  quadrants, positron flow into the  $(-x, +y)$  direction in the  $(-x, +z)$  quadrants, electron flow into the  $(-x, -y)$  direction in the  $(+x, -z)$  quadrants and positron flow into the  $(+x, +y)$  direction in the  $(+x, -z)$  quadrants are dominant. The  $X$ -type layer along the separatrix region is also characteristic. Figure 2*b* shows the  $y$ -component of the positron current. The current is strong around the  $O$ -type region, while it is weak or reversed in the very center of the  $O$ -type region, where the plasma density is at a maximum. Around the reconnecting region, there is a broadened structure of weak  $y$ -current. The most characteristic thing is the inclined current layer along the lower side of the separatrix, which is indicated by the dashed lines. This inclined layer corresponds to one of the  $X$ -type density regions in Figure 2*a*. The electron current structure is upside down; it is slightly inclined in the counter-clockwise direction and it is on the upper side of the separatrix. In ion-electron plasmas, several simulations of guide field reconnection reported an inclined electron current layer (Horiuchi & Sato 1997; Drake et al. 2003; Hesse et al. 2004; Pritchett & Coroniti 2004) near the  $X$ -type region. However, the ion current layer is hardly recognized due to the ion’s large spatial scale. In our simulation, we observe both current layers for positrons and electrons. Positrons are driven by the reconnection electric field  $E_y$  around the  $X$ -type region, and then they tend to escape in the lower right (or upper left) direction along 3D reconnected field lines. Similarly, electrons tend to escape from the  $X$ -type region; they tend to escape in the upper right (or lower left) direction. Therefore, there is charge non-neutrality around the outflow region (Fig. 2*c*). Positrons are localized in the lower right side of the reconnection region. Figure 2*d* shows the reconnection electric field  $E_y$ . Its typical amplitude is  $E_y/B_0 \sim (0.05 - 0.1)$  around the  $X$ -type region and it is substantially weaker than antiparallel case;  $E_y/B_0 \sim (0.2 - 0.3)$ . The  $E_x$  component is comparable or slightly larger than  $E_y$ , but consistent with plasma inflows. Its typical value is  $E_x/B_0 \sim 0.1$  in the upper inflow region and  $E_x/B_0 \sim -0.1$  in the lower inflow region. The vertical electric field is substantially large:  $E_z/B_0 \sim 0.7$  in Figure 2*e*. It is consistent with the outflow jet and guide magnetic field  $B_y$ , which is compressed around the  $O$ -type region. The non-neutral charge distribution is consistent with the  $E_z$  structure, too.

Figure 3 shows the energy spectra over the main simulation domain. As reconnection evolves, particle acceleration takes place and then the high-energy tail continues to grow. The late-time spectrum at  $t/\tau_c = 200$  is quasi-stable. Although it is difficult to discuss the spectral index in such a temporally and spatially limited system, the power-law index is  $\sim -2.9$  in the last stage.

In order to study particle acceleration, we track the trajectories of the highest energy positrons, whose energy exceeds  $40mc^2$  at  $t/\tau_c = 100$  (indicated by gray shading in Fig. 3). Over the entire simulation domain they are only found along the inclined current layer,



both in the upper left side and in the lower right side in the reconnection region. The high-energy electrons are found in the other current layer. Gray points in Figure 4a show spatial distribution of selected positrons around the lower right current layer. We pick up two typical trajectories from  $t/\tau_c = 0$  to  $t/\tau_c = 200$ , which are indicated by solid lines in Figure 4. We call them positron A and positron B, respectively. The diamond or circle signs show their positions at  $t/\tau_c = 100$ . Positron A belongs to the majority. Starting from the left outside the presented region, the positron visits the  $X$ -type region and then escapes toward the lower right, gyrating around the reconnected field lines. The path is along the inclined positron current layer. While it travels a long distance in the  $y$ -direction, the particle mainly gains its energy from the reconnection electric field  $E_y$  near the  $X$ -type region. Notice that the scaling of the  $y$ -direction is extremely larger than the  $x$ - and  $z$ -directions in Figure 4b. The energy gained from  $E_x$  and  $E_z$  is substantially low. Positron B is a rare sample. It starts near the center and then it moves into the  $X$ -type region. As reconnection goes on, it travels in the  $y$ -direction along the  $X$  line in the  $x$ - $z$  plane because it is trapped by the guide field  $B_y$  around the  $X$  line. At  $t/\tau_c = 200$ , it still rotates around the  $X$  line and its energy increases from  $40.8mc^2(t/\tau_c = 100)$  to  $75.5mc^2(t/\tau_c = 200)$ . The acceleration continues until it finds a way to escape toward the upper left or the lower right.

In the antiparallel reconnection, the reconnection electric field  $E_y$  is a main player of particle acceleration, too. Note that the reconnection electric field is perpendicular to the magnetic field lines in the antiparallel case,  $\mathbf{E} \cdot \mathbf{B} \sim 0$ . Therefore, particle acceleration occurs in the acceleration region where the frozen-in condition is never satisfied ( $|\mathbf{E}| > |\mathbf{B}|$ ; Zenitani & Hoshino (2001)), or in the piled-up regions where the electro-magnetic fields have strong peaks (ZH07). In the present case of guide field reconnection, particle acceleration occurs because  $\mathbf{E} \cdot \mathbf{B} \neq 0$  around the reconnection region. The guide field  $B_y$  traps the particles, preventing them from escaping in the  $x$ - or  $z$ -directions, so that they are accelerated by  $E_y$ . The particle acceleration occurs even when they gyrate around the magnetic field lines, because it relies on the parallel electric field  $E_{\parallel}$ .

We have also compared the nonlinear evolutions of two-dimensional reconnection runs with various guide field amplitudes. Generally speaking, as the guide field increases, signatures of guide field reconnection become more apparent; electron/positron flows become separated, and then the inclined current layers and charge separation structure appear. The reconnection electric field also becomes weaker because outflow jets becomes slower. In addition, in spontaneous or nearly spontaneous cases, it takes a longer time until the nonlinear reconnection process breaks up, as the stronger guide field is imposed.

Figure 15 compares the acceleration efficiency in various reconnection runs. The ratio of the nonthermal kinetic energy to the total kinetic energy are presented as a function of time.

The ratio is calculated from the energy spectra in the same way as ZH07 (Appendix A in ZH07); we assume an equivalent energy spectra of the relativistic Maxwellian distribution, which carries the same amount of kinetic energy as the energy spectra in simulations, and then we obtain the nonthermal kinetic energy by subtracting the equivalent thermal spectra from the simulation spectra in their high-energy tail. This method may underestimate the amount of the nonthermal energy, but we can quantitatively compare the acceleration efficiency in a simple way. In Figure 15, the simulation time for run R3-A ( $|B_y/B_0| = 0.5$ ), in which the trigger force is slightly weak, is re-arranged by  $\Delta t = 35\tau_c$  so that we can directly compare it to the other cases. Here we focus on the two-dimensional (2D) reconnection runs; we discuss the 3D results later again in §5.2. Roughly speaking, the acceleration efficiency seems to decrease as the guide field increases. The antiparallel run (run R3) is the most efficient accelerator among the three runs. The maximum accelerated energy is also a function of the guide field during the similar timescale (See Table 1). This is due to its strong reconnection electric field  $E_y \sim 0.3B_0$ , and the reconnection electric field  $E_y$  becomes weaker in the guide field cases. In run R3-C, the “acceleration region” nearly smears out due to the weak reconnection field  $E_y \sim 0.1B_0$ . On the other hand, the trapping effect of the guide field contributes to the acceleration efficiency. Even though particle acceleration by  $E_\perp$  becomes less active, parallel acceleration by  $E_\parallel$  works instead. Thus, guide field reconnection (run R3-C) still produces a substantial amount of nonthermal energy  $\sim 15\%$ . Considering the limitation of our simple method, more kinetic energy will be carried by nonthermal particles. In general, guide field reconnection seems to be an efficient particle accelerator, which releases more than 15%-30% of the plasma energy into the nonthermal kinetic energy.

In run R3-A, we notice that the secondary particle acceleration takes place in the very late stage (at  $t/\tau_c \gtrsim 250$ ), and then particles are accelerated up to  $\gamma \sim 200$ . The spectral index evolves to a harder value of  $\sim -2.2$  in the very late stage (at  $t/\tau_c = 400$ ). Since periodic boundary effects arise in that late stage, particle acceleration may be enhanced due to interactions with the multiple reconnection structures. The secondary acceleration is only found in the weak guide field case (run R3-A), and so its long-term evolution needs further investigation.

When we compare runs R3-D and R3-C ( $|B_y/B_0| = 1.5$ ), the system evolution in run R3-D delays by approximately  $145\tau_c$ - $150\tau_c$  in terms of the global energy distribution. In run R3-D, we observe six tearing islands around  $t/\tau_c = 200$ , and then they start to collide with each other until one reconnection region dominates around  $t/\tau_c = 300$ . The O-type islands often have onion-ring density structure, and the X-type current layers connect to the outermost rings. However, the global energy evolution and the acceleration efficiency are almost the same. They seem to be rather insensitive to the initial evolution whether

the system evolves from forced single reconnection or from multiple tearing islands, in the moderate guide field cases of  $|B_y/B_0| \sim 1.5$ .

#### 4. 3D EVOLUTION WITH NO GUIDE FIELD

In this section, we study the 3D evolution of the current sheet in antiparallel configuration. We look at the simulation results of run 3D-A. As stated in §2, we imposed small external electric fields around the center, but the trigger fields are not strong enough to force reconnection.

We briefly review the linear evolution, which was discussed in our previous paper (ZH05b). Figure 5a is a snapshot at  $t/\tau_c = 80$ . The current sheet is between the two gray surfaces and the plasma density at the neutral plane ( $z = 0$ ) is projected into the bottom wall, with color shading from black (empty) to red (dense;  $n = 1.2n_0$ ). Figure 6 presents the  $E_y$  structure at  $t/\tau_c = 80$ . The red regions have the positive polarity of  $E_y > 0$ , while the blue regions are negative:  $E_y < 0$ . Apparently these profiles exhibit a quasi 2D evolution of the RDKI. One can see the polarity change along the  $x$ -axis in the  $x$ - $z$  plane (the right surfaces in Fig. 6), but this is due to small  $y$ -displacement of the structure. The wave-number of the RDKI is  $k_y\lambda \sim 0.74$  (mode 3), while mode 4 is observed in the relevant 2D run D3. However, both mode 3 and mode 4 are reasonable with the linear theories. The observed growth rate  $\tau_c\omega_i = 0.06$  is slightly slower than the expected rate  $\tau_c\omega_i \sim 0.1$ , but it is still faster than that of the relativistic tearing instability.

Figures 5b and 5c show the nonlinear development of the current sheets at  $t/\tau_c = 110$  and 140. The current sheet is strongly folded at  $t/\tau_c = 110$ , and then its wave fronts start to collide each other. At  $t/\tau_c = 110$ , the gray density surfaces are reset to  $n = 1/3n_0$ , so that we can see the low-density hole around the center. We discover that magnetic reconnection takes place in this central hole. Figure 5d is a zoomed-in view around the neutral plane at  $t/\tau_c = 110$ . The gray lines are magnetic field lines, traced from the following six start points:  $(x, y, z) = (-5, 0, -0.5), (-5, 2, -0.5) \cdots (-5, 10, -0.5)$  in units of  $\lambda$ . Magnetic field lines are reconnected around the central low-density region. Contrary to the 2D reconnection in the  $x$ - $z$  plane, reconnection structure involves the  $x$ - $y$  plane, because the current sheet is highly folded by the RDKI. Plasma inflows mainly come from the  $\pm y$ -directions, and then outflows flow into the  $\pm x$ -direction. Inflows from the  $\pm z$ -direction are difficult to identify. Interestingly, the central reconnection region contains multiple field reversals between the folded current sheets. Since plasmas are expelled away from the reconnection region, there is a low-density hole around the central region. The reason reconnection takes place in the center may be the initial trigger impact. Around the central region, the RDKI is invoked

earlier than other locations, and then the folded structure first appears there. Reconnection occurs in such a well-developed folded region. In this simulation, the central reconnection region is finally overwhelmed by the current sheet corruption, and then the system evolves into the turbulent state at  $t/\tau_c = 140$ . This is consistent with the 2D RDKI picture. The  $x$ - $y$  cross sections of the plasma density structure in the upper wall indicate the plasma mixing across the double periodic boundaries. Eventually, most energy in the system is converted into plasma heat, 2 times hotter than the original state. Particle acceleration by the RDKI or reconnection is negligible.

## 5. 3D EVOLUTION WITH GUIDE FIELD

Next, we study a 3D evolution of the current sheet with a guide field in run 3D-B. The guide field amplitude is  $|B_y/B_0| = 0.5$ . All other conditions are the same as those of run 3D-A in §4. Throughout the simulation run ( $0 \leq t/\tau_c \leq 220$ ), the total energy is conserved within an error of 0.6%.

### 5.1. Linear Evolution: Relativistic Drift Sausage/Kink Tearing Instability

First, we study the linear structure of the mode in detail. Compared with run 3D-A, the current sheet seems to be more stable in the early stage. It takes  $t/\tau_c \sim 100$  until we observe visible changes in the current sheet. At  $t/\tau_c = 120$ , we observe a purely growing flute like mode in the oblique direction on the upper side of the current sheet in Figure 7a. We think this is a generalized mode between the relativistic tearing instability and the RDKI-type instabilities (ZH05b). The mode is  $(1, 1)$  or its wavevector is  $\mathbf{k}_1\lambda = (0.25, 0.25)$ . The two panels in Figure 8 show the plasma density slices at  $z = \pm\lambda$ . We see the structure with  $\mathbf{k}_1$  on the upper side of the current sheet at  $z = \lambda$ , while we observe another oblique mode  $(1, -1) : \mathbf{k}_2\lambda = (0.25, -0.25)$  on the lower side of the current sheet at  $z = -\lambda$ . On both sides, it seems that the oblique lines are slightly disconnected around  $(x, y) \sim (\pm 12.8\lambda, 0)$ . Probably the fastest growing modes do not match the system size, and then they adjust into the nearest periodic mode  $(1, \pm 1)$ . Therefore, it takes a longer time before we observe the visible change. The most powerful Fourier modes are  $(1, \pm 1)$  in the simulation data, and Figure 9 shows  $z$ -profiles of the density perturbation of the two modes. The amplitude of the two modes is nearly same, but their peaks are in the other side of the current sheet. We confirmed that these oblique perturbations are purely growing unstable modes. Carrying out a supplemental 2D PIC simulation under the same conditions in that particular angle, we observe similar a similar asymmetric profile, mode  $(2, \pm 2)$ , while we obtain mode  $(1, \pm 1)$

in run 3D-B.

In order to study the nature of the instability, we have also calculated eigen profiles of the oblique instability in the current sheet by using the relativistic two-fluid theory. We assume the perturbation of  $\delta f \propto f(z) \exp(ik_x x + ik_y y + \omega_i t)$  as introduced in §3.1, and then we consider the oblique case of  $k_x, k_y \neq 0$ . In Figure 10, the eigen functions for  $k_x \lambda = 0.25$ ,  $k_y \lambda = 0.25$  and  $B_y/B_0 = -0.5$  are presented as functions of  $z$ . Perturbed magnetic field profiles ( $\delta B_x, \delta B_y, i\delta B_z$ ) and electric field profiles ( $\delta E_x, \delta E_y, i\delta E_z$ ) employ the same normalization. The other three panels display the current profiles ( $\delta J_x, \delta J_y, i\delta J_z$ ), the bulk velocity perturbations ( $i\delta V_{+x}, i\delta V_{+y}, \delta V_{+z}$ , where  $\delta \mathbf{V}_+ = \delta \mathbf{v}_p + \delta \mathbf{v}_e$ ), and density profiles ( $\delta D_+ = \delta d_p + \delta d_e$  and  $\delta D_- = \delta d_p - \delta d_e$ ) are normalized by their maximum values. The current profiles ( $\delta J_x, \delta J_y, i\delta J_z$ ) are calculated from other perturbed values:  $\delta D_+, \delta \mathbf{V}_-$ , where  $\delta \mathbf{V}_- = \delta \mathbf{v}_p - \delta \mathbf{v}_e$ . These profiles are consistent with the simulation data. For example, the density perturbation  $\delta D_+$  in Figure 10 is in excellent agreement with the relevant perturbation in simulation data in Figure 9. In general, the perturbation profiles are not symmetric nor anti-symmetric with  $z$ . As observed in  $\delta B_x$  or  $\delta D_+$ , the mode seems to be substantially localized in the upper half of  $z > 0$ . The other mode ( $\mathbf{k}_2$ ;  $k_x \lambda = 0.25, k_y \lambda = -0.25$ ) has an opposite structure; it is localized in the lower half of  $z < 0$ .

Figure 11 schematically illustrates the structure of the oblique mode ( $\mathbf{k}_1$ ). Although we called this mode relativistic drift-kink tearing instability (RDKTI) in ZH05b, we find that the structure is rather similar to that of the relativistic drift sausage instability (RDSI), a cousin mode of the RDKI. Therefore, we shall rename it relativistic drift-sausage tearing instability (RDSTI). For simplicity, we assume that the perturbed structure is localized in the upper half of the current sheet in the top panel in Figure 11. In addition, the two conventional instabilities in antiparallel configuration; the RDSI/RDKI and the relativistic tearing instability are illustrated in the bottom panels of Figure 11. The small arrows represent the perturbed vectors. The phase of the linear perturbation is set to zero at the origin. Therefore, the dashed line in the neutral sheet is phase  $\pi$  and the imaginary perturbations (phases  $\pi/2$  and  $3\pi/2$ ) are found between the origin and the dashed line. The dashed line (phase  $\pi$ ) in the neutral plane is equivalent to the  $X$ -line of the tearing mode. If we look at the eigen profiles in the upper vicinity of the neutral plane ( $z \gtrsim 0$ ), plasma bulk inflow into the  $X$  line ( $-\delta v_z < 0$ ), the diverging outflows in  $i\delta v_{x,y}$ , the perpendicular magnetic field  $i\delta B_z$ , and the current enhancement  $J_y$  are all consistent with the those of the tearing mode. In addition, roughly speaking, the density  $\delta D_+$  is positive in the  $O$ -like region and negative in the  $X$ -like region. The reconnection electric field  $E_y$  is positive around the  $X$  line, although it not strong enough to penetrate into the lower half domain. There is also  $E_z$  structure in  $i\delta E_z$ , which is between the  $X$ - and  $O$ -type regions. The  $E_z$  structure and the relevant charge separation in  $i\delta D_-$  are signatures of the guide field tearing mode or guide

field reconnection, as presented in Figures 2*c* and 2*e*.

Next, we compare the perturbed structure with that of the RDSI/RDKI in the  $y$ - $z$  plane. We compare the eigen profiles with those of the RDKI and the RDSI, which are presented in Figures 14 and 21 in ZH07. In both cases of the RDSTI and the RDSI, the two-peak structure in density profile  $\delta D_+$  stands for sausage-type modulation, while reverse peaks stand for kink-type modulation. The charge separation and  $E_z$  structure of the RDSTI is well connected to the those of the RDSI. One specific feature of the RDSTI is the perturbed plasma flow structure. The flow direction changes as a function of  $z$ , and then the flow is parallel to the background magnetic field in the topmost layer. Overall, the structure of the RDSTI is complicated, but it is well consistent with the relevant 2D instabilities. The RDKTI has almost same structure as the RDSTI, except that perturbation is kink-like in the lower side of the current sheet in the  $y$ - $z$  plane.

We investigate the eigen modes over various parameters: the guide field amplitude  $B_y/B_0 = 0, -0.5, -1, -1.5$  and the wavevectors of ( $0 \leq k_x\lambda \leq 1, 0 \leq k_y\lambda \leq 1$ ). Their fastest growth rates ( $\tau_c\omega_i$ ) are presented in contour maps in top panels in Figure 12. We take  $\Delta k_{x,y}\lambda = 0.05$  so that  $21^2$  parameters per map are presented. All of the modes are purely growing. Due to the mathematical symmetry, we can obtain eigen modes and growth rates for  $(k_x, k_y)$  from their counterparts in  $(|k_x|, |k_y|)$ . We repeat the validity of our linear theory again. As discussed in §3.1, our two-fluid approximation will be valid only in the long-wavelength range (e.g.  $|k_y\lambda| \lesssim 0.7$  for the RDKI/RDSI). Therefore, the results in Figure 12 will be reliable only when  $|k\lambda| \lesssim 0.7$ . The bottom panels in Figure 12 show the type of the fastest eigen mode. By comparing the peak-structure in their density profiles, we classify the obtained fastest eigen modes into the following three types: kink type (A in Fig. 12), sausage type (B), and neither of them (C). The tearing mode is classified in sausage-type modes, because its density perturbation is symmetric with the neutral plane ( $z = 0$ ). Notice that both kink-type mode and sausage-type mode coexist in the same point, and that we discuss the type of the fastest mode in the specific parameter range. It seems that the RDKI/RDKTI is faster only in the shorter wavelength region along the  $k_y$ -axis. In the other region, the RDSI/RDSTI replaces the RDKI/RDKTI.

In the guide field case of  $B_y/B_0 = -0.5$ , the RDKI/RDSI along the  $k_y$ -axis is stabilized by the magnetic tension of the guide field as discussed in §3. The oblique RDSTI modes, which are along the background magnetic field lines, survive instead. Some oblique modes grow even faster in the guide field case because they are weakly stabilized by the magnetic tension in antiparallel case. As the guide field becomes stronger, the most dominant modes change direction, in accordance with the background magnetic field lines. Since the RDKI/RDSI component of the instability is driven by the  $\mathbf{k}$ -aligned component of the

current, the growth rates of the oblique modes decrease. On the other hand, growth rates of the tearing mode component seems to be rather insensitive to  $|B_y/B_0|$ . In the strong guide field case of  $|B_y/B_0| \gtrsim 1$ , we can no longer classify some oblique modes to kink-type or sausage-type modes (C in Fig. 12). These modes are highly localized on one side of the current sheet, and their perturbation is very small on the other side of the current sheet.

## 5.2. Nonlinear Evolution

After the linear stage, the current sheet becomes very thin at several points, where two RDSTI/RDKTI modes compress the current sheet from the upper and lower sides. The thinning point evolves into a big plasma hole at the center of the simulation box at  $t/\tau_c = 170$  in Figure 7b. The secondary magnetic reconnection takes place there. Once reconnection breaks up, it continues to grow. Figure 13 shows a 2D slice at  $y = 0$  at  $t/\tau_c = 170$ . The upper panel shows the typical reconnection structure. The outflow velocity is up to  $0.6c$ , which is between the antiparallel case ( $0.8c$ ) and the strong guide field case ( $0.4c$ ) of  $B_y/B_0 = -1.5$ . The typical inflow velocity is  $\sim 0.1c$ . The current sheet still looks similar to a Sweet-Parker current sheet, but careful observation shows several signatures of the guide field reconnection. The bottom panel shows the positron current structure in color and the  $E_z$  structure in contour, respectively. The positron current layer is slightly inclined in a clockwise direction. However, the electron current layer is inclined in a counter clockwise direction. So, the two current layers coexist in a Sweet-Parker-like current sheet. In addition, the vertical electric field  $E_z$  is not negligible. Its amplitude is  $\sim 0.4B_0$  in the right side and  $\sim -0.4B_0$  in the left side, while the typical reconnection electric field is  $E_y \sim 0.17B_0$ . The  $x$  component of the inflow electric field is  $E_x \sim \pm 0.05B_0$ . These signatures are almost same in the relevant 2D run: run 3D-A. The width (in  $y$ ) of the reconnection region seems to be limited by the scale of the system or the scale length of the oblique modes. Figure 7c shows a snapshot at  $t/\tau_c = 200$ . The oblique bridges are blown away from the neutral sheet due to the intense plasma pressure, and then the dense points around  $(x, y) \sim (0, \pm 12.8\lambda)$  are no longer observed. In addition, plasmas are drawn into the central reconnecting point, and there is a plasma hole along the  $X$  line:  $x = 0, z = 0$ . The typical speed of reconnection jets is up to  $\sim 0.71c$ . Figure 7d is the last snapshot of our simulation at  $t/\tau_c = 220$ . The system structure is highly turbulent, but we observe the filament-like structures in the  $y$ -directions. Considering that reconnection dissipates the field energy of antiparallel magnetic fields, it is reasonable that we observe structures which are threaded by the guide field  $B_y$ .

After magnetic reconnection occurs, the magnetic energy tends to be converted to the nonthermal part of the plasma kinetic energy, due to the particle acceleration around the

reconnection region. Figure 14 compares the energy spectra in the system for two 3D runs and the relevant 2D runs of guide field reconnection. The initial state of two 3D runs is almost similar to the spectrum of run 3D-B at  $t/\tau_c = 140$  (Fig. 14, *dotted line*). In the case of run 3D-A (*bold line*), plasma energy is converted into plasma heat, due to magnetic dissipation by the RDKI. The nonthermal tail of the spectrum ( $\varepsilon \gtrsim 30mc^2$ ) is slightly enhanced due to the particle acceleration. The footpoint of the nonthermal tail is approximately same as that of the 2D RDKI case, but the tail itself is not as apparent as in the 2D case. Due to the irregularity along the  $x$ -direction or other 3D effects, particle acceleration by the RDKI works less effectively than the ideal 2D case. In the case of run 3D-B, the energy spectrum is almost unchanged until relativistic reconnection breaks up. At  $t/\tau_c = 140$  (Fig. 14, *dotted line*), plasmas are slightly heated by 3% from the initial state. In the late stage of  $t/\tau_c = 220$  (Fig. 14, *dash-dotted line*), the nonthermal tail is enhanced due to the particle acceleration by reconnection. The nonthermal slope is well-described by the power law with the index of  $-2.8$  in a range of  $8 < \varepsilon/mc^2 < 20$ . This is nearly same as the spectral index in the 2D runs. The power-law spectral index is  $\sim -2.7$  at  $t/\tau_c = 200$  in run R3-A, and  $\sim -2.9$  at  $t/\tau_c = 200$  in run R3-C.

The time history of the nonthermal ratio parameter, the ratio of plasma nonthermal energy to plasma kinetic energy, is presented in Figure 15. In the case of run 3D-A (Fig. 15, *thick line*), there is a small peak after  $t/\tau_c = 80$  due to the  $dc$  acceleration by the RDKI, but eventually the nonthermal ratio is less than 2%. This is consistent with 2D simulations on the RDKI, which reports the nonthermal ratio of far less than 5% (ZH07). However, in the case of run 3D-B (Fig. 15, *thick dashed line*), shortly after the central reconnection region appears at  $t/\tau_c = 170$ , more than 14% of the kinetic energy consists of the nonthermal energy. This ratio is approximately half of the value in the relevant 2D run (run R3-A; Fig. 15, *thin gray line*). We think this is due to the limited volume of reconnection region in 3D configuration. For example, along the neutral line ( $X = 0$ ) at  $t/\tau_c = 200$  (Fig. 7c), reconnection and the relevant particle acceleration is active around the center  $y \sim 0$ , while we do not observe reconnection flow structure around  $y/\lambda \sim \pm 12.8$ . Since reconnection can utilize half of the system volume along the  $y$  direction, the nonthermal ratio is small in run 3D-B, compared with the 2D counterpart (run R3-A). If we employ larger simulation box to reduce the periodic limitation in the  $y$ -direction, we may observe wider reconnection region and then the nonthermal ratio may increase. Anyway, run 3D-B more efficiently generates the nonthermal energy than the antiparallel case of run 3D-A, because underlying physical mechanism is completely different. Most of magnetic energy is dissipated into the thermal energy by the RDKI in the anti-parallel case (run 3D-A). However, in the guide field case (run 3D-B) a substantial amount of magnetic energy is dissipated into the nonthermal component of plasma kinetic energy, associated with magnetic reconnection.



## 6. DISCUSSION

First, we discuss the system evolution in an antiparallel configuration. We are interested in which process dominates, the reconnection or the RDKI, because it greatly changes the energy distribution in the system; reconnection involves nonthermal particle acceleration, but the RDKI leads to plasma heating. Comparison of linear growth rates (ZH07) suggested that the RDKI dominates in the relativistic regime of  $T/mc^2 \gtrsim 1$ . Our results in §4 basically support this argument. Although we imposed the external trigger force, it was not strong enough to evoke reconnection before the RDKI modulates the current sheet. The *dc* acceleration by relativistic reconnection is not likely to evolve; then magnetic dissipation and plasma heating by the RDKI would be the main signature of a relativistic current sheet. However, we discovered small reconnection regions inside the folded current sheet structure. The reconnection generates a density hole around the center, and then the density hall may evolve into a global reconnection structure in the larger system. It is true that the RDKI grows faster than the reconnection in our relativistic regime of  $T/mc^2 \sim 1$ , but once reconnection is initiated, we do not know whether it overwhelms the outside RDKI structures.

Next, we discuss the guide field effect on the system evolution. We showed that the RDKI is completely stabilized by the finite amount of the guide field in §3. We do not yet understand how much guide field is necessary to stabilize the RDKI, but we expect that reconnection mode dominates again under the guide field conditions. In §5, we showed that the evolution is more complicated than expected. We considered the oblique instabilities (RDSTI/RDKTI) to understand the linear evolution of the current sheet. They grow in two oblique directions (e.g.  $\mathbf{k}_1$  and  $\mathbf{k}_2$ ), which can be interpreted as twin extensions of the conventional RDSI/RDKI. In the antiparallel case the kink-type mode dominates, and there were no signatures of sausage-type modes. In the guide field case, we found that the sausage-type branch (RDSTI) dominates in run 3D-B. In some sense this is quite reasonable, because both the RDSI and the tearing instability modulate the current sheets in a symmetric way with the neutral plane, while the RDKI modulates the current sheets in an asymmetrical way. On the other hand, since the RDSTI/RDKTI have asymmetric structure and since they always appear as twins in the guide field cases, it does not matter whether the oblique modes are sausage-like or kink-like. The important point is that the twin oblique modes, whose wave fronts are parallel to the twisted background magnetic fields, initiates magnetic reconnection. Since relativistic guide field reconnection involves particle acceleration, the guide field turns on the nonthermal particle acceleration in the 3D system. When we impose a stronger guide field, one can see that an angle between two RDKTI/RDSTI branches ( $\mathbf{k}_1$  and  $\mathbf{k}_2$ ) becomes wider in accordance with the lobe magnetic field lines. The RDSTI/RDKTI slow down, but their growth rates are still faster than the relativistic tearing instability (Fig. 12). Under the extreme guide field condition, since the dominant RDSTI/RDKTI modes

are inclined to the  $\pm x$ -directions, coupling between two oblique waves may directly lead to quasi-2D growth of the tearing instability.

On the system size limitation, the late-time evolution of our 3D runs may be somewhat artificial, due to the periodic boundary effects. In run 3D-A, magnetic diffusion is enhanced by the plasma transport across the double periodic boundaries in  $z$ . In run 3D-B, the oblique mode (RDSTI) seems to be bounded by the system length. Since we see the remnant of the other modes (Fig. 8), we probably failed to observe the most unstable modes. However, as long as similar oblique modes dominate they will trigger the secondary magnetic reconnection in the similar way. If we set larger simulation box, do we observe multiple reconnection points in accordance with the spatial structure of the RDSTI/RDKTI? If so, how are particles accelerated in multiple reconnection regions? Or does the  $X$  line extend and then does the system evolve into the 2D reconnection? Furthermore, recent and ongoing works on large-scale evolution of magnetic reconnection exhibit more dynamical behaviors than expected (e.g. plasmoid formation and collisions; Daughton & Karimabadi (2007)). Large-scale, 3D evolution of relativistic pair plasma reconnection still remains an open issue, regardless of the presence of the guide field. Future simulations may reveal various dynamical behaviours beyond our linear and early nonlinear results.

Regarding the particle acceleration in the guide field reconnection, we studied particle acceleration by the parallel electric field  $E_{\parallel}$  in the 2D case, and we observed similar acceleration signatures in the 3D case, too. In general, as long as we investigated we observed nonthermal energy spectra with indexes of  $-2 \sim -3$  by magnetic reconnection, regardless of the amplitude of guide field, in both 2D and 3D cases. The upper limit of the accelerated energy remains to be solved, or it seems unlimited as long as reconnection continues to consume magnetic energy. We confirmed that maximum lepton energy easily exceeds the Lorentz factor of 80-200 (40-100MeV; see Table 1). This will also be influenced by large-scale evolution of the system.

Let us briefly discuss potential astrophysical applications, based on physical insights from our results. In pulsar winds with relativistically hot pair plasmas (Coroniti 1990; Lyubarsky & Kirk 2001; Kirk & Skjæraasen 2003), it is unlikely that current sheets contain substantial amount of guide fields because magnetic field lines are highly striped or toroidal. Therefore, plasma heating by the RDKI is the most likely process, unless plasma temperature drops down to nonrelativistic one. On the contrary, in the AGN context, magnetic reconnection is quite likely to involve the guide field component. Several authors demonstrated electron acceleration due to the field-aligned electric field  $E_{\parallel}$  by means of test particle simulations (Schopper et al. 1998; Nodes et al. 2003). We demonstrated that relativistic particle acceleration by  $E_{\parallel}$  in a fully self-consistent way, including feedbacks from accelerated

electrons and other kinetic effects, and so our results provide a theoretical proof of the ultra relativistic particle acceleration in the MeV/GeV range, at least in electron-positron pair plasma reconnection. In the case of soft gamma repeaters, it is unclear how giant flares occur at magnetars. The present models discuss the crustal “quakes” (Thompson & Duncan 1995, 2001) or the flux tube corruption in analogy with solar flares and coronal mass ejections to trigger giant flares. In addition, the tearing instability in the force-free magnetar corona is proposed to explain the subsequent bursting activities (Lyutikov 2003). In these models, magnetic energy is stored in a magnetic spiral in the star core or the flux lobes, or coronal magnetic shear. Therefore, once a flare occurs, it is likely that magnetic reconnection involves a magnetic shear or out-of-plane magnetic field. The guide field reconnection will occur, and reconnection will be a yet another favorable source of nonthermal particles as well as ultra-relativistic shock fronts.

Recently, relativistic MHD models have been developed to investigate astrophysical plasma problems. Our results warn that an MHD approximation is no longer valid in the case of relativistic guide field reconnection. As plasma outflow becomes an order of  $c$ , charge separation structure becomes apparent in the outflow region, and then it breaks down the charge neutral assumption of one-fluid theory. Instead, multi-fluid simulations, which deal with positively charged fluids and negatively charged fluids independently, are favorable to study with guide field reconnection problems.

Let us summarize this paper. First, we investigated how the guide field affects 2D instabilities; the RDKI is stabilized by a finite amount of the guide field, while the reconnection/tearing mode is rather insensitive to the guide field. Then, we studied the nonlinear evolution of relativistic guide field reconnection. Characteristic field structure and particle acceleration process were investigated. Next, we studied 3D evolution of the current sheet. As predicted by 2D studies, the RDKI dominates and dissipates the magnetic energy, but we also discovered that reconnection occurs inside the folded current sheet. Finally, we studied 3D evolution with a guide field condition. The properties of the oblique RDSTI/RDKTI mode and the nonlinear evolution of secondary reconnection is discussed, in association with the 2D counterparts. Due to the guide field, nonthermal particle acceleration, which generates power-law energy spectra with an index of  $-2 \sim -3$ , occurs in the relativistic pair plasmas. Our results show that the guide field reconnection is a favorable acceleration engine in high-energy astrophysical plasmas.

The authors express their gratitude to T. Yokoyama, M. Hesse, I. Shinohara, P. L. Pritchett and Y. E. Nakagawa for helpful comments. The author is also grateful to the anonymous referee for helping to improve this manuscript. This work was supported by the facilitates of JAXA and the Solar-Terrestrial Environment Laboratory, Nagoya University.

## REFERENCES

- N. Bessho and A. Bhattacharjee 2005, *Phys. Rev. Lett.* , 95, 245001
- N. Bessho and A. Bhattacharjee 2007, *Phys. Plasmas* , 14, 056503
- G. T. Birk, A. R. Crusius-Wätzel and H. Lesch 2001, *Astrophys. J.* , 2001, 559, 96
- J. Birn, J. F. Drake, M. A. Shay, B. N. Rogers, R. E. Denton, M. Hesse, M. Kuznetsova, Z. W. Ma, A. Bhattacharjee, A. Otto and P. L. Pritchett 2001, *J. Geophys. Res.* , 106, 3715
- E. G. Blackman and G. B. Field 1994, *Phys. Rev. Lett.* , 72, 494
- M. Brittnacher, K. B. Quest and H. Karimabadi 1995, *J. Geophys. Res.* , 100(A3), 3551
- F. V. Coroniti 1990, *Astrophys. J.* , 349, 538
- W. Daughton 1999, *J. Geophys. Res.* , 104, 28701
- W. Daughton and H. Karimabadi 2007, *Phys. Plasmas* , 14, 072303
- T. di Matteo 1998, *MNRAS* , 299, L15
- J. F. Drake and Y. C. Lee 1977, *Physics of Fluids*, 20, 1341
- J. F. Drake, M. Swisdak, C. Cattell, M. A. Shay, B. N. Rogers and A. Zeiler 2003, *Science*, 299, 873
- G. Drenkhahn 2002, *Astron. Astrophys.* , 387, 714
- G. Drenkhahn and H. C. Spruit 2002, *Astron. Astrophys.* , 391, 1141
- M. Hesse, K. Schindler, J. Birn and M. Kuznetsova 1999, *Phys. Plasmas* , 6, 1781
- M. Hesse, M. Kuznetsova and J. Birn 2004, *Phys. Plasmas* , 11, 5387
- M. Hesse and S. Zenitani 2007, *Phys. Plasmas* , 14, 112102
- M. Hoshino 1987, *J. Geophys. Res.* , 92, 7368
- R. Horiuchi and T. Sato 1997, *Phys. Plasmas* , 4, 277
- J. D. Huba 2005, *Phys. Plasmas* , 12, 012322
- C. H. Jaroschek, H. Lesch and R. A. Treumann 2004a, *Astrophys. J.* , 605, L9

- C. H. Jaroschek, R. A. Treumann, H. Lesch and M. Scholer 2004b, *Phys. Plasmas* , 11, 1151
- I. Katanuma and T. Kamimura 1980, *Physics of Fluids*, 23, 2500
- J. G. Kirk and O. Skjæraasen 2003, *Astrophys. J.* , 591, 366
- D. A. Larrabee, R. V. E. Lovelace and M. M. Romanova 2003, *Astrophys. J.* , 586, 72
- H. Lesch and G. T. Birk 1997, *Astron. Astrophys.* , 324, 461
- H. Lesch and G. T. Birk 1998, *ApJ*, 499, 167
- Y. Lyubarsky and J. G. Kirk 2001, *ApJ*, 547, 437
- Y. Lyubarsky 2005, *MNRAS* , 358, 113
- M. Lyutikov 2003, *MNRAS* , 346, 540
- M. Lyutikov and D. Uzdensky 2003, *Astrophys. J.* , 589, 893
- M. Lyutikov 2006, *MNRAS* , 367, 1594
- F. C. Michel 1982, *Reviews of Modern Physics*, 54, 1
- F. C. Michel 1994, *Astrophys. J.* , 431, 397
- C. Nodet, G. T. Birk, H. Lesch and R. Schopper 2003, *Phys. Plasmas* , 10, 835
- P. L. Pritchett and F. V. Coroniti 2004, *J. Geophys. Res.*, 109, 1220
- K. B. Quest and F. V. Coroniti 1981, *J. Geophys. Res.* , 86, 3289
- P. Ricci, G. Lapenta and J. U. Brackbill 2003, *Phys. Plasmas* , 10, 3554
- M. M. Romanova and R. V. E. Lovelace 1992, *Astron. Astrophys.* , 262, 26
- M. Scholer, I. Sidorenko, C. H. Jaroschek, R. A. Treumann and A. Zeiler 2003, *Phys. Plasmas* , 10, 3521
- M. A. Shay, J. F. Drake, B. N. Rogers and R. E. Denton 2001, *J. Geophys. Res.* , 106, 3759
- K. Shibata, S. Masuda, M. Shimojo, H. Hara, T. Yokoyama, S. Tsuneta, T. Kosugi and Y. Ogawara 1995, *Astrophys. J.* , 451, L83
- R. Schopper, H. Lesch and G. T. Birk 1998, *Astron. Astrophys.* , 335, 26
- I. Silin and J. Büchner 2003, *Phys. Plasmas* , 10, 3561

- B. U. O. Sonnerup, G. Paschmann, I. Papamastorakis, N. Sckopke, G. Haerendel, S. J. Bame, J. R. Asbridge, J. T. Gosling and C. T. Russell 1981, *J. Geophys. Res.* , 86, 10049
- C. Thompson and R. C. Duncan 1995, *MNRAS* , 275, 255
- C. Thompson and R. C. Duncan 2001, *Astrophys. J.* , 561, 980
- D. A. Uzdensky and A. I. MacFadyen 2006, *Astrophys. J.* , 647, 1192
- N. Watanabe and T. Yokoyama 2006, *Astrophys. J.* , 647, L123
- L. M. Zelenyi and V. V. Krasnoselskikh 1979, *Astronomicheskii Zhurnal*, 56, 819
- S. Zenitani and M. Hoshino 2001, *Astrophys. J.* , 562, L63
- S. Zenitani and M. Hoshino 2005a, *Astrophys. J.* , 618, L111
- S. Zenitani and M. Hoshino 2005b, *Phys. Rev. Lett.* , 95, 095001
- S. Zenitani and M. Hoshino 2007, *Astrophys. J.* , 670, 702

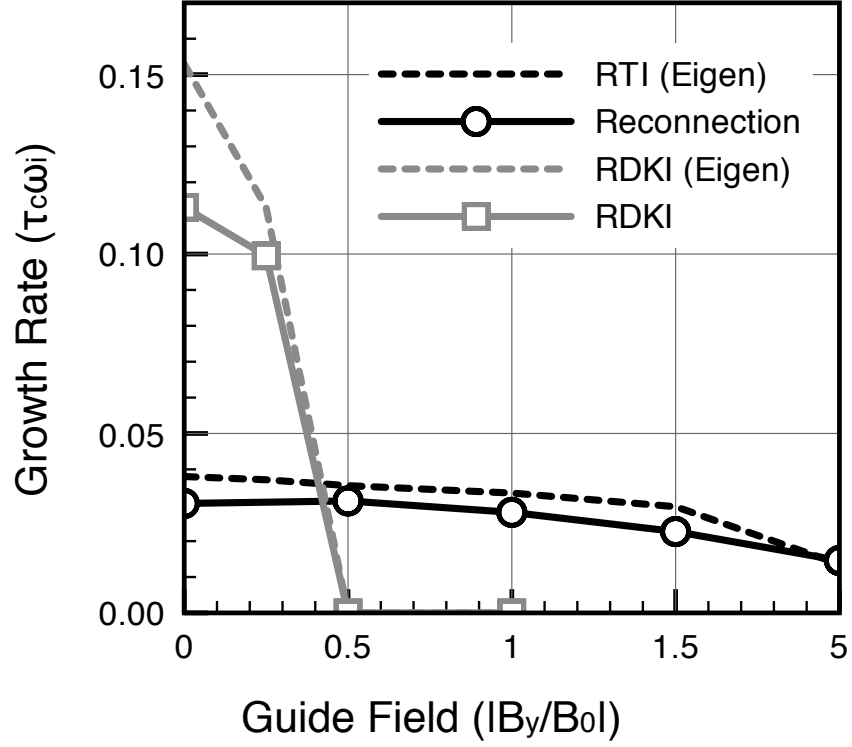


Fig. 1.— Guide field dependence ( $|B_y/B_0|$ ) of the growth rate  $\omega_i$ , normalized in the light transit time  $\tau_c$ . The fastest eigen growth rate of the relativistic tearing instability, linear growth rate of the fastest growing modes in relativistic magnetic reconnection, eigen growth rate of typical RDKI, and linear growth rate of the RDKI are shown.

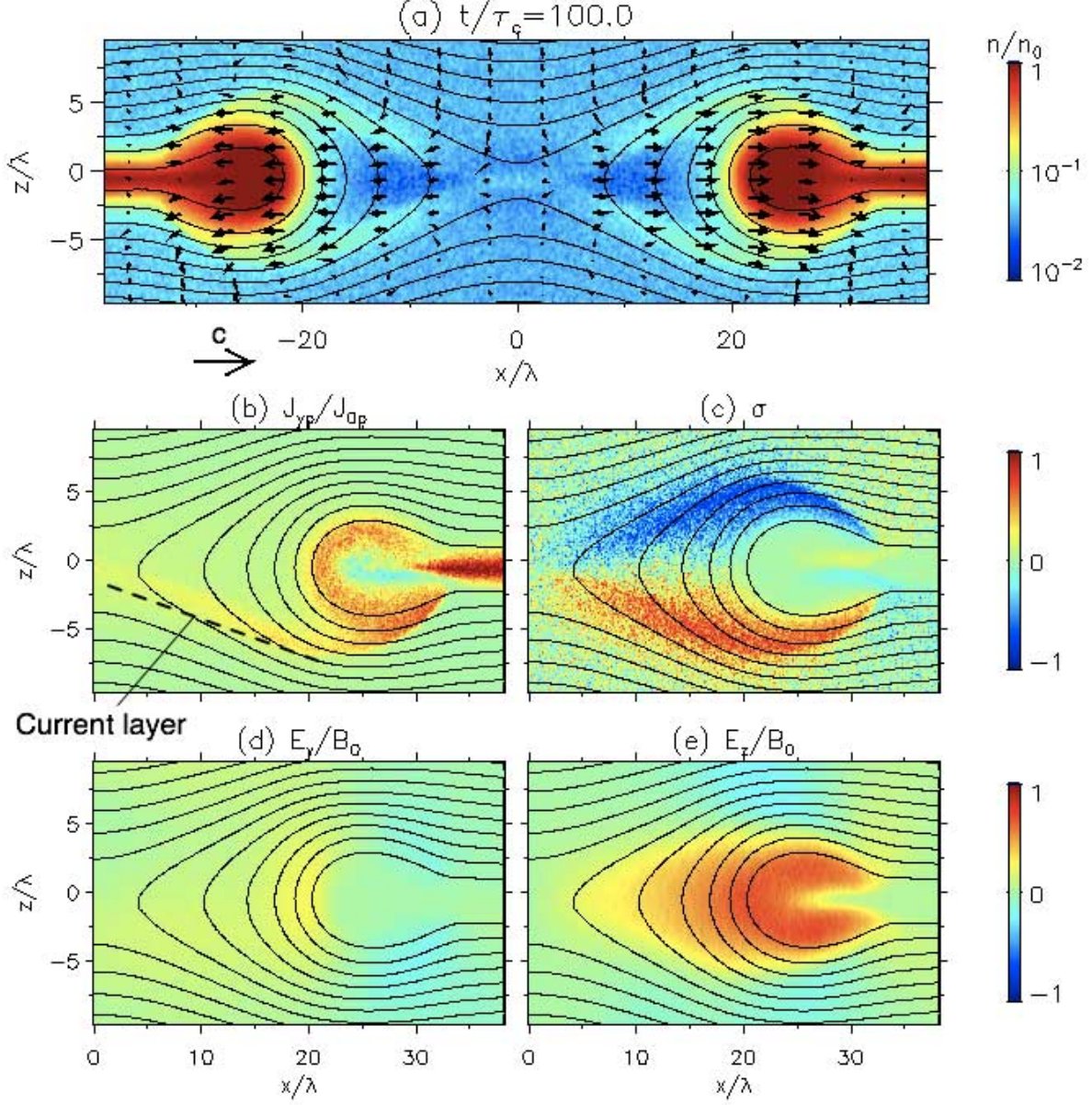


Fig. 2.— Snapshots of run R3-C ( $|B_y/B_0| = 1.5$ ) at  $t/\tau_c = 100.0$ . (a) Plasma density and flows, (b) positron current density  $J_{yp}$ , (c) charge non-neutrality [ $\sigma = [n_p - n_e]/[n_p + n_e]$ ], (d) reconnection electric field  $E_y$ , and (e) vertical electric field  $E_z$  are presented, respectively. The background counter lines show the magnetic field lines in the  $x$ - $z$  plane.



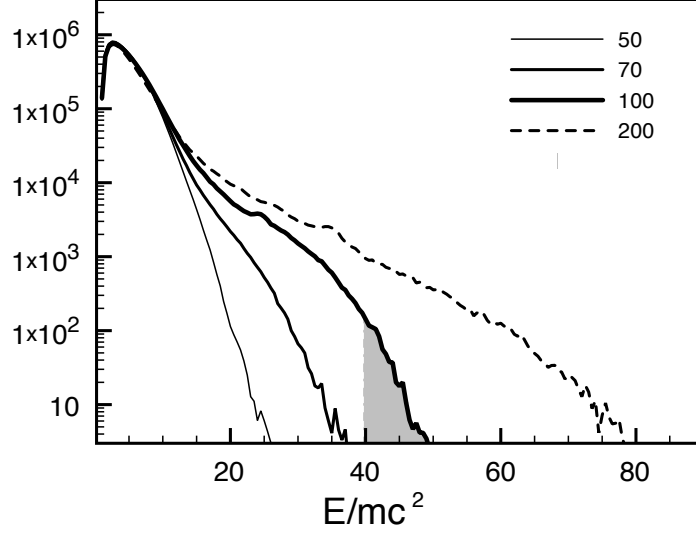


Fig. 3.— Energy spectra of run R3-C at characteristic stages:  $t/\tau_c = 50, 70, 100$ , and  $200$ .

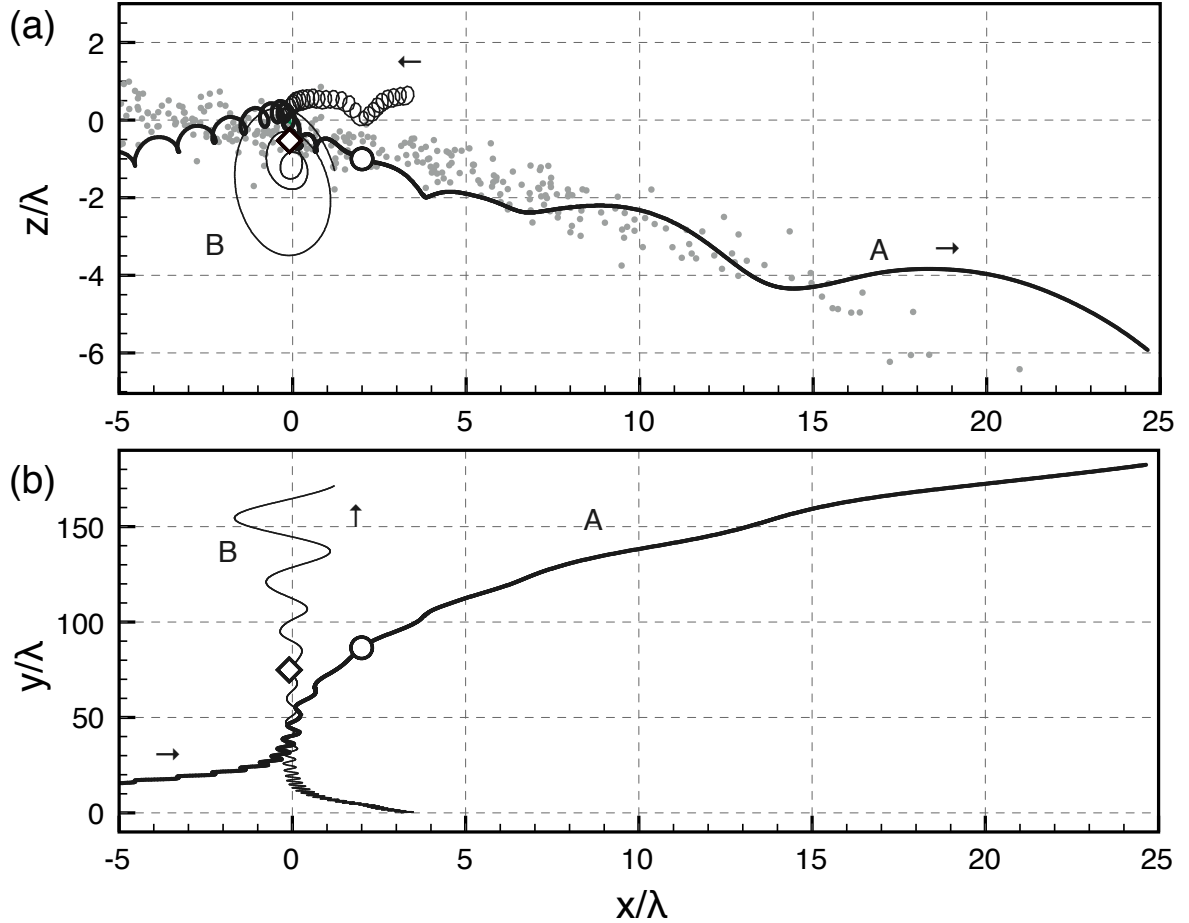


Fig. 4.— (a) Spatial distribution of high-energy particles (*gray points*;  $\varepsilon \geq 40mc^2$ ) at  $t/\tau_c = 100$ . Two typical trajectories are projected in the same plane. The signs show the relevant positions at  $t/\tau_c = 100$ . (b) Trajectories in the  $x$ - $y$  plane.

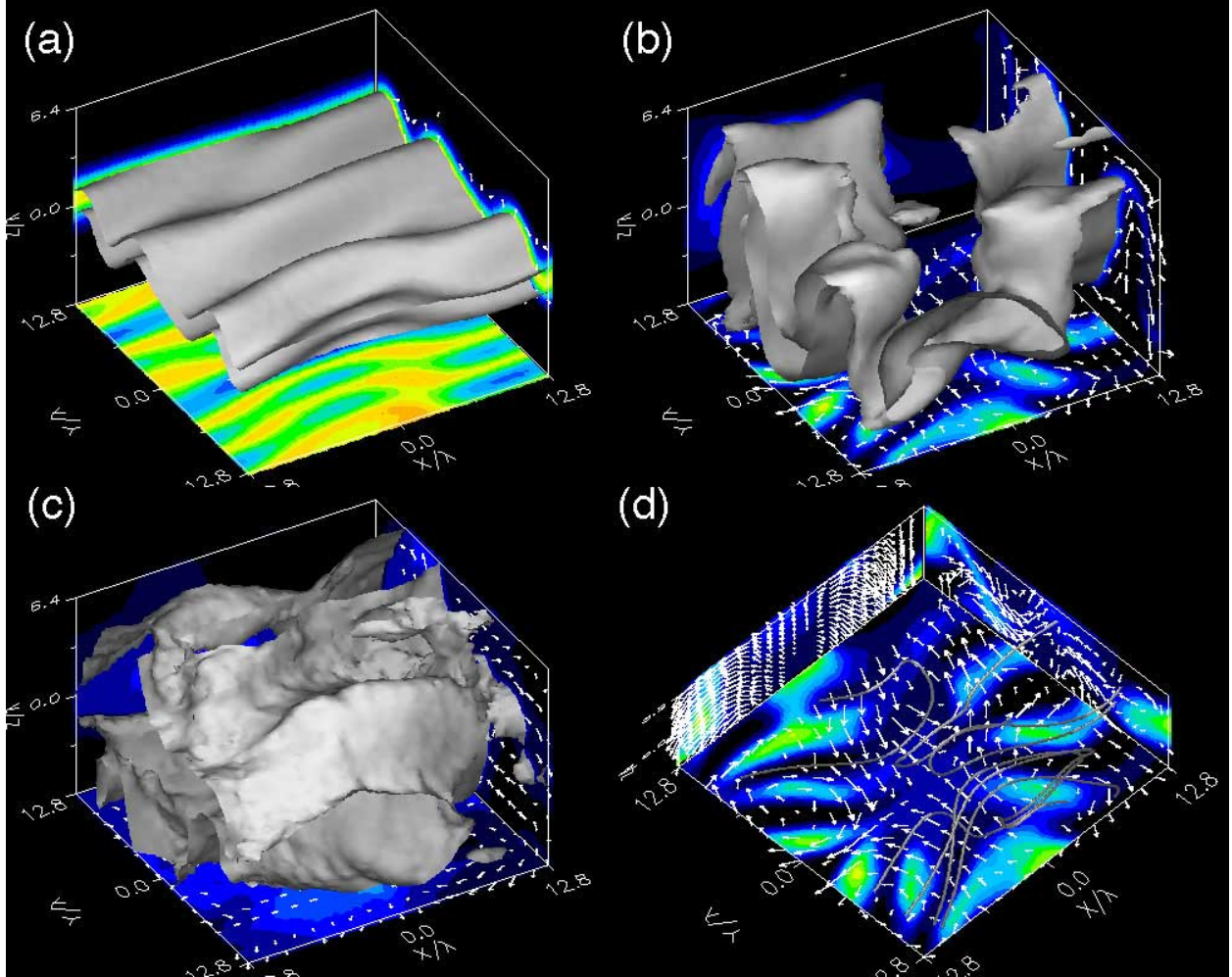


Fig. 5.— Snapshots of the current sheet in run 3D-A at (a)  $t/\tau_c = 80$ , (b) 110 and (c) 140. The gray surfaces show the density surface of (a)  $n = 2/3n_0$ , (b)  $n = 1/3n_0$ , and (c)  $n = 1/5n_0$ , respectively. The plasma density at the neutral plane ( $z = 0$ ) is projected into the bottom wall, with color from black (empty) through blue (sparse) to red (dense;  $n \sim 1.2n_0$ ). Panel (d) is a zoomed-in view around the neutral plane ( $-3.2 < z/\lambda < 3.2$ ) at  $t/\tau_c = 110$ . The gray lines trace the magnetic field lines. The plasma flow in the 2D planes ( $x = 0, y = 0$ , and  $z = 0$ ) are presented as white arrows in the three walls. The light speed ( $v = c$ ) is projected to the arrow length 4.

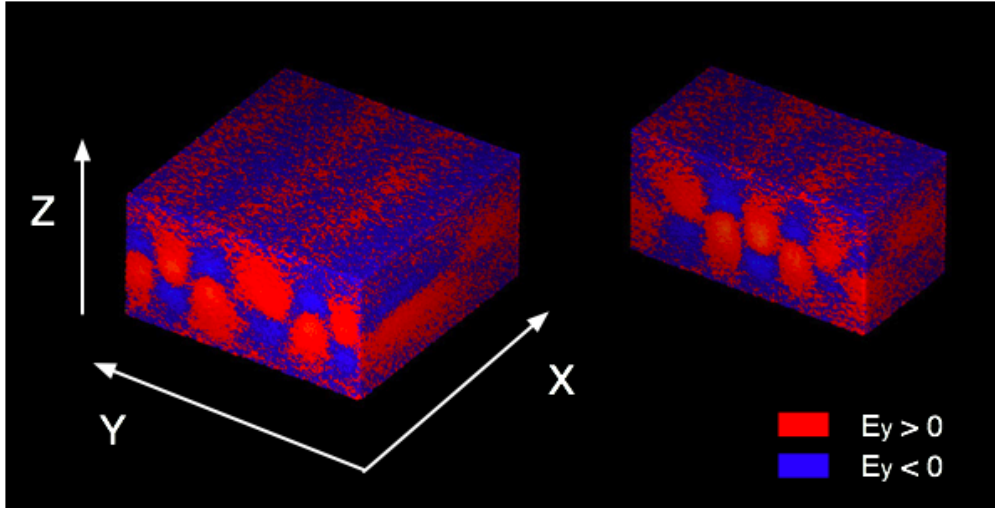


Fig. 6.— The  $E_y$  structure in run 3D-A at  $t/\tau_c = 80$ .

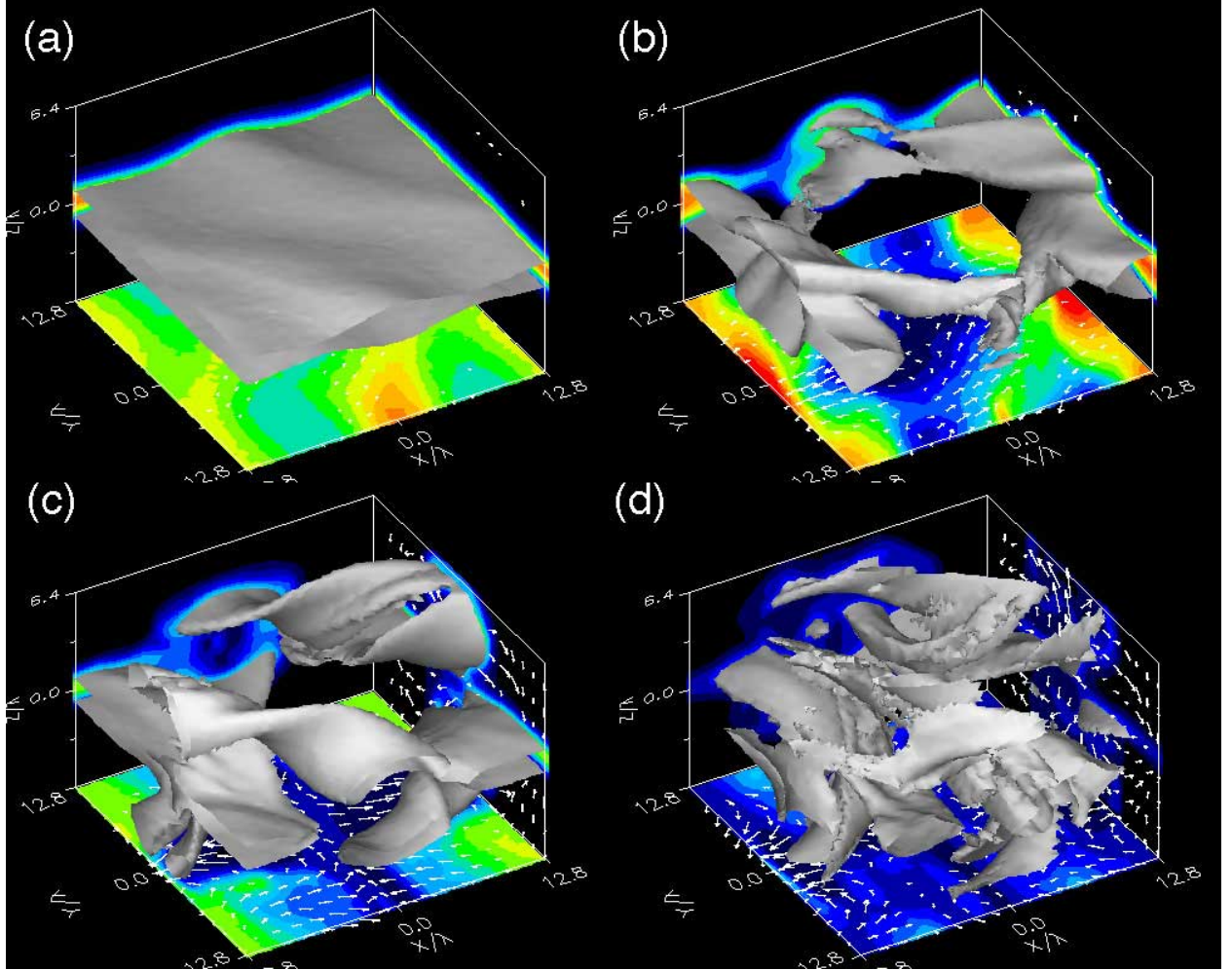


Fig. 7.— Snapshots of the current sheet in run 3D-B with a guide field configuration ( $B_y/B_0 = -0.5$ ) at (a)  $t/\tau_c = 120$ , (b) 170, (c) 200 and (d) 220. Gray surfaces show the plasma density of (a)  $n = 2/3n_0$ , (b)  $2/3n_0$ , (c)  $1/2n_0$  and (d)  $1/3n_0$ , respectively. The bottom walls show the plasma density structure in/under the neutral plane at (a-b)  $z = -\lambda$  or at (c-d)  $z = 0$ .

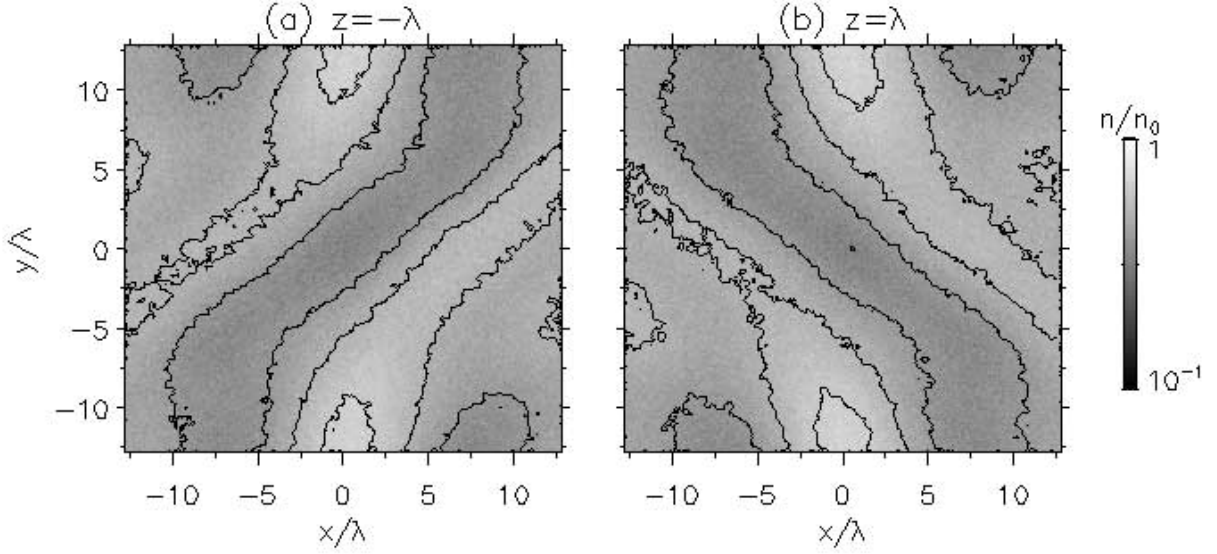


Fig. 8.— Slices of the simulation domain in run 3D-B at  $t/\tau_c = 120$ . The plasma density is represented by gray shading.

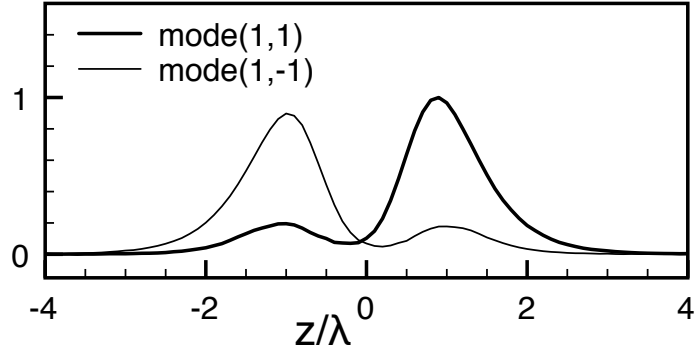


Fig. 9.— The  $z$ -profiles of the density perturbation in run 3D-B at  $t/\tau_c = 120$ . Two dominant modes (1,1) and (1,-1) are presented.

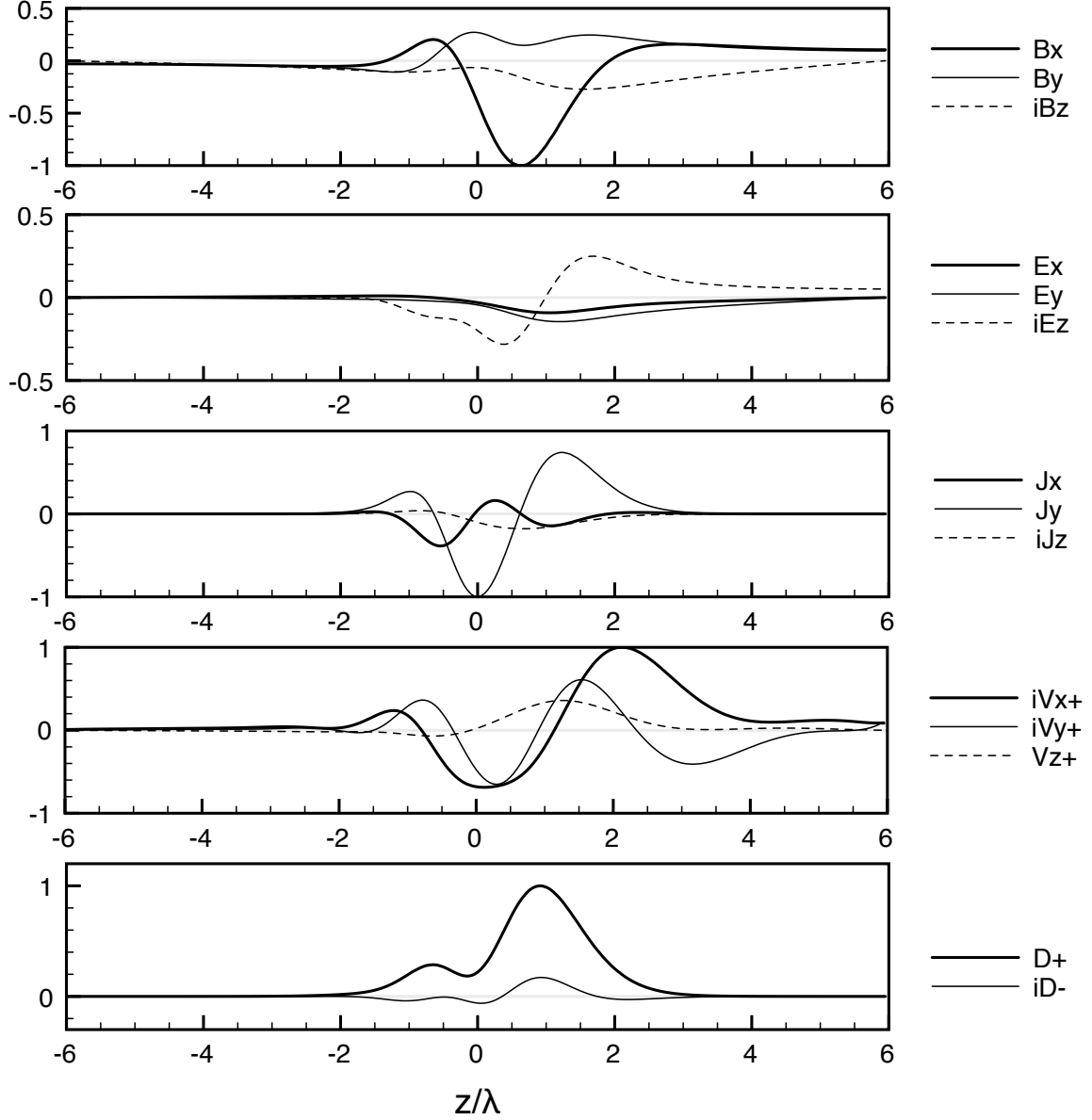


Fig. 10.— Typical eigen functions of the relativistic drift-sausage tearing instability as a function of  $z$ , for the normalized wavenumbers  $k_x\lambda = 0.25$  and  $k_y\lambda = 0.25$ . Perturbed magnetic fields:  $\delta B_x, \delta B_y, i\delta B_z$ ; electric fields:  $\delta E_x, \delta E_y, i\delta E_z$ ; electric currents:  $\delta J_x, \delta J_y, i\delta J_z$ ; bulk velocities:  $i\delta V_{+x}, i\delta V_{+y}, \delta V_{+z}$ ; and density fluctuations:  $\delta D_{\pm} = \delta d_p \pm \delta d_e$  are presented, respectively.

### 3D Relativistic Drift-Sausage (or Drift-Kink) Tearing Instability

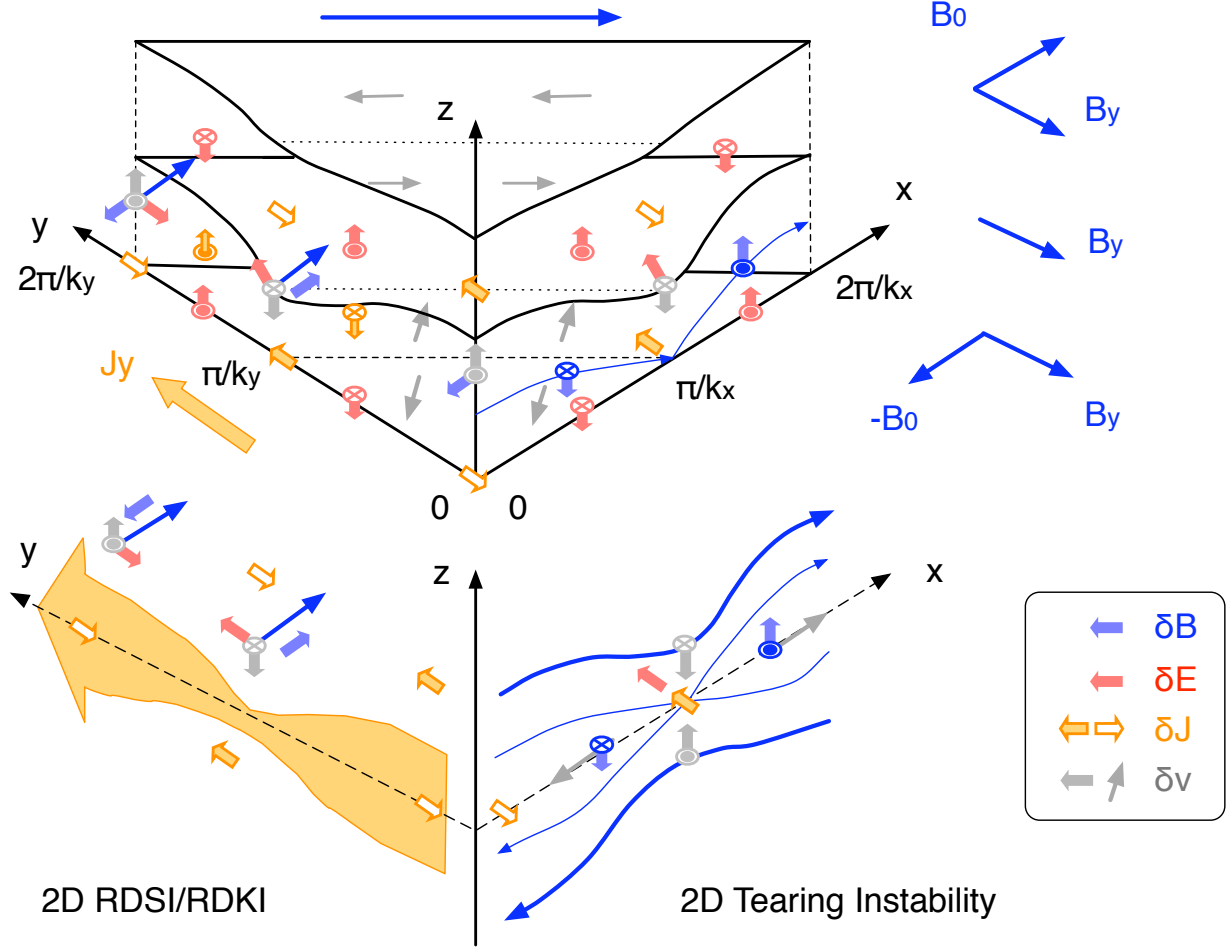


Fig. 11.— Schematic illustration of the 3D relativistic drift-sausage tearing instability. Bottom panels show the relevance to the conventional 2D instabilities.

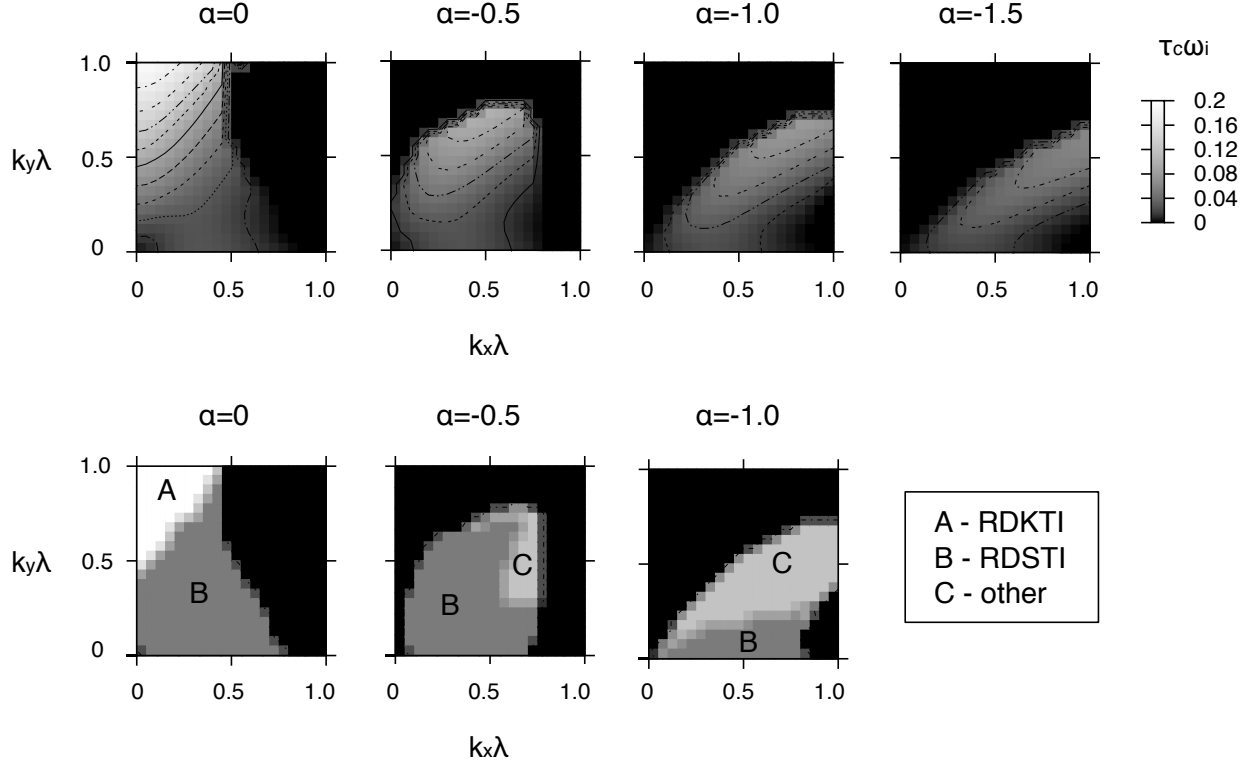


Fig. 12.— *Top*: Growth rate ( $\tau_c \omega_i$ ) of the instabilities in wavevector spaces of ( $0 \leq k_x \lambda \leq 1, 0 \leq k_y \lambda \leq 1$ ), as a function of the guide field amplitude  $B_y/B_0 = \alpha = 0, -0.5, -1, -1.5$ . *Bottom*: Three classes of the unstable modes are mapped; A: kink-type modes; B: sausage-type modes; and C: others (neither or intermediate).



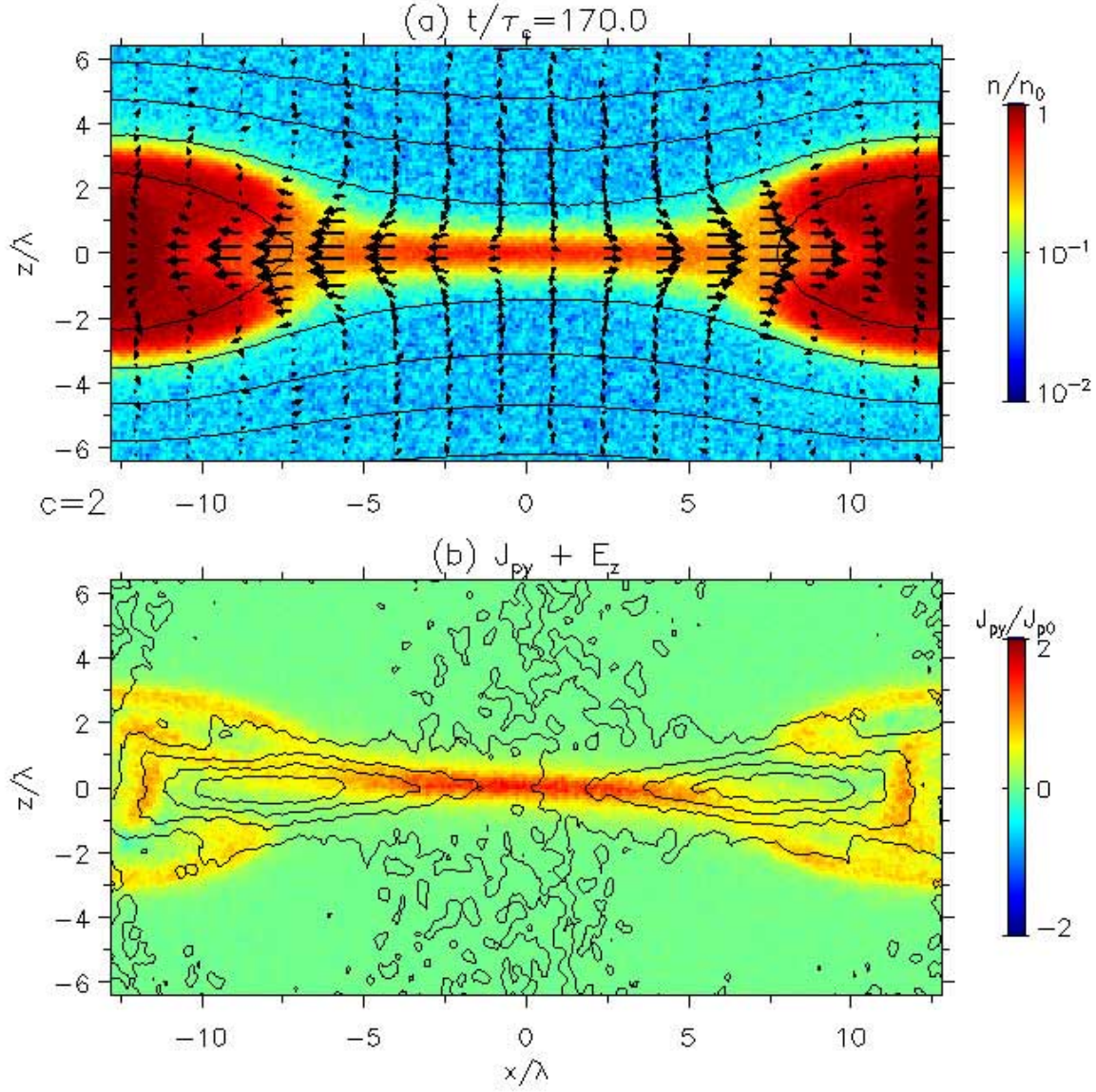


Fig. 13.— Snapshots of 2D cut plane at  $y = 0$  in run 3D-B at  $t/\tau_c = 170$ . (a) Plasma density, flows, 2D magnetic field lines and (b) positron current  $J_{py}$  (colored shading), vertical electric field  $E_z$  (contours) are presented. The contour step  $\Delta E_z$  is set to  $0.1B_0$ .

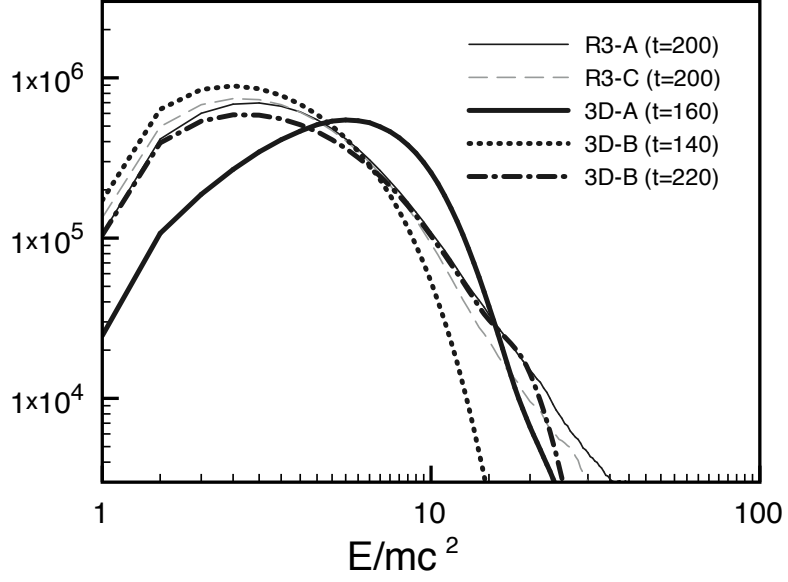


Fig. 14.— Energy spectra of 3D/2D runs. Plasma count number for 3D runs are re-arranged for comparison with 2D runs.

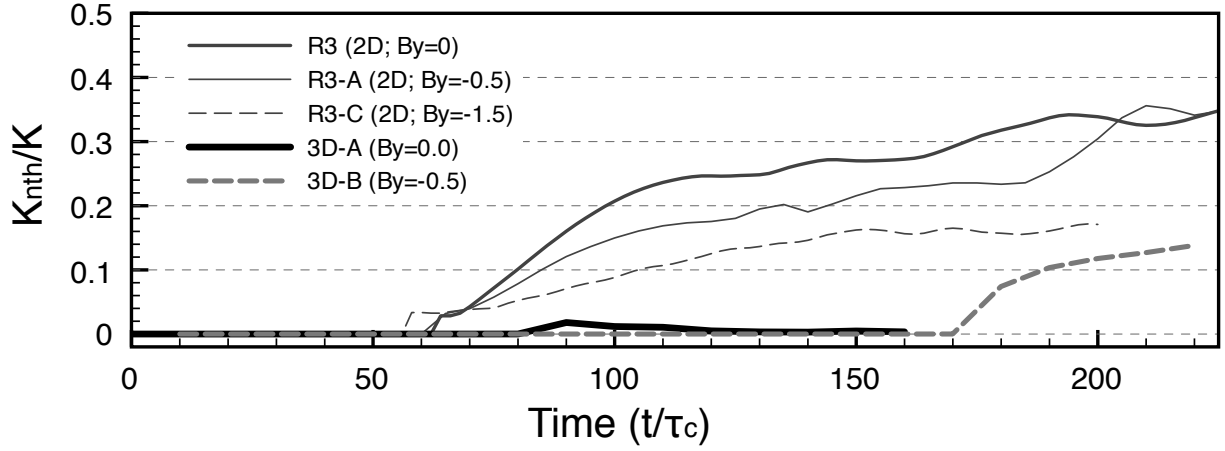


Fig. 15.— Time histories of nonthermal ratio parameters for reconnection runs; runs R3, R3-A, R3-C, 3D-A and 3D-B.

Table 1. List of Simulation Runs

Run	$L_x$	$L_y$	$L_z$	$B_y/B_0$	$n_{bg}/(\gamma\beta n_0)$	$n_{tot}$	$K_{nth}/K$	$\tau_c\omega_i$	$\gamma_{max}$	Type
R3	102.4	—	51.2	0	5%	$1.7 \times 10^7$	$> 3.7 \times 10^{-1}$	$3.0 \times 10^{-2}$	$> 158$	F
R3-A	102.4	—	51.2	-0.5	5%	$1.7 \times 10^7$	$> 4.0 \times 10^{-1}$	$3.1 \times 10^{-2}$	$> 122$ ( $\sim 210$ )	S*
R3-B	102.4	—	51.2	-1.0	5%	$1.7 \times 10^7$	$> 1.7 \times 10^{-1}$	$2.8 \times 10^{-2}$	$> 80$	S*
R3-C	102.4	—	51.2	-1.5	5%	$1.7 \times 10^7$	$1.7 \times 10^{-1}$	$2.3 \times 10^{-2}$	$> 86$	F
R3-D	102.4	—	51.2	-1.5	5%	$1.7 \times 10^7$	$> 1.8 \times 10^{-1}$	$2.3 \times 10^{-2}$	$> 79$	S
R3-E	102.4	—	51.2	-5.0	5%	$1.7 \times 10^7$	—	$1.5 \times 10^{-2}$	$> 42$	S*
D3	—	25.6	51.2	0	0	$4.2 \times 10^6$	$7.2 \times 10^{-2}$	$1.1 \times 10^{-1}$	48	S
D3-A	—	25.6	51.2	-0.25	0	$4.2 \times 10^6$	—	$1.0 \times 10^{-1}$	38	S
D3-B	—	25.6	51.2	-0.5	0	$4.2 \times 10^6$	—	N/A	22	S
D3-C	—	25.6	51.2	-1.0	0	$4.2 \times 10^6$	—	N/A	22	S
3D-A	25.6	25.6	25.6	0	5%	$5.4 \times 10^8$	$1.8 \times 10^{-2}$	$6 \times 10^{-2}$	52	S*
3D-B	25.6	25.6	25.6	-0.5	5%	$5.4 \times 10^8$	$> 1.4 \times 10^{-1}$	—	$> 45$	S*

Note. — Initial parameters and obtained physical values of simulation runs. R3, D3, and 3D runs are 2D simulations for magnetic reconnection, 2D simulations for the RDKI, and 3D simulations, respectively. The system width  $L_x$  is assumed to be in the oblique direction ( $x$ - $y$ ). The system size ( $L_x, L_y, L_z$  in units of  $\lambda$ ), the guide field amplitude ( $B_y/B_0$ ), the ratio of the background plasma density ( $n_{bg}$ ) to the plasma density in the current sheet ( $\gamma\beta n_0$ ), the total number of the particles ( $n_{tot}$ ), the nonthermal ratio ( $K_{nth}/K$ ) the linear growth rate ( $\tau_c\omega_i$ ) and the Lorentz factor of the highest energy particle ( $\gamma_{max}$ ) are presented.